EES Solar

Accepted Manuscript

This article can be cited before page numbers have been issued, to do this please use: A. Singh and A. Gagliardi, *EES Sol.*, 2025, DOI: 10.1039/D5EL00040H.

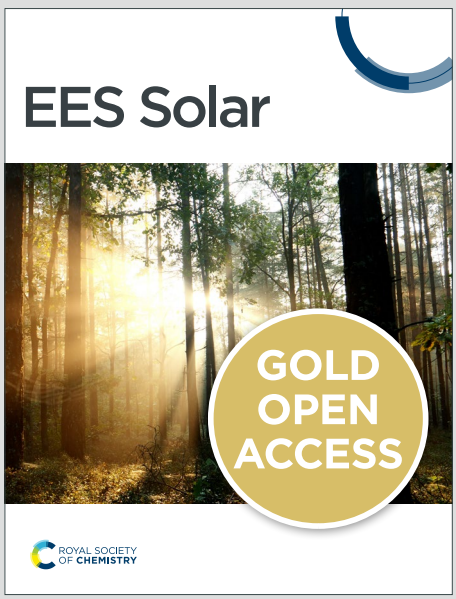

EL-REV-03-2025-000040.R2 - Drift-diffusion modeling of perovskite solar cells: past and future possibilities

Broader context Statement

Perovskite solar cells (PSCs) have rapidly advanced as one of the most promising solar cell technologies due to high efficiency (exceeding 27%), low-cost fabrication and tunable optoelectronic properties. Despite huge potential, PSCs' commercialization is hampered by low stability, J-V hysteresis, and grain boundaries-led performance degradations. Drift-diffusion (DD) modeling has emerged as a vital tool for investigating and optimizing PSC performance, offering insights into charge carrier dynamics that are difficult to probe experimentally. This review provides a comprehensive and critical evaluation of DD modeling approaches in PSCs, highlighting their strengths, limitations, and opportunities for improvement. Strategies to refine DD modeling by incorporating advanced sub-models for degradation, ionic trappings, mobility, grain boundaries, photon recycling, and quantum effects are presented. Furthermore, the possibility to combine time/frequency domain analysis, density functional theory and machine learning approaches is presented to improve the accuracy and reliability of DD modeling to predict short and long-term performance degradations. The broader impact of this work lies in its potential to identify current gaps and proposing future directions to guide the development of robust, scalable, and physically grounded DD models for PSCs.

View Article Online
DOI: 10.1039/D5EL00040H

EES Solar

REVIEW

Cite this: DOI: 00.0000/xxxxxxxxxx

Drift-diffusion modeling of perovskite solar cells: past and future possibilities

Ajay Singh*[a] and Alessio Gagliardi[b]

Received Date
Accepted Date

DOI: 00.0000/xxxxxxxxxx

Approaching 27% of power-conversion efficiency and offering solution processability, perovskite solar cells (PSC) have paved a path to high-efficiency and cost-effective solar cell technologies. Despite huge potential, PSC's commercialization is hampered by low stability, J-V hysteresis, and grain boundaries-led performance degradation. Drift-diffusion (DD) modeling has become an indispensable tool for investigating underlying device physics and various dynamical phenomena that are difficult to understand solely by experimental techniques. However, most of the proposed DD models rely on oversimplified assumptions and approximations, and therefore do not mimic the actual device while modeling the role of interfaces, doping, mobilities, ionic migration, device architecture, and J-V hysteresis. Moreover, a significant gap remains in modeling short-term and long-term performance degradation. This review critically examines the evolution of DD modeling in PSCs, highlighting its strengths, limitations, and opportunities for improvement. We discuss strategies to enhance model accuracy by incorporating advanced sub-models for degradation, ionic trappings, mobility, grain boundaries, photon recycling, and quantum effects. We emphasize the incorporation of generation/annihilation of ionic defects, and combining time/frequency domain analysis to predict short and long-term performance degradations. For the modeling parameters inaccessible via experiments, a possibility to combine DD and Density Functional Theory (DFT) is explored. Furthermore, we present how machine learning models and interfacing experimental data can help speeding up and in improving accuracy and reliability of DD models. By identifying current gaps and proposing future directions, this review aims to guide the development of robust, scalable, and physically grounded DD models for PSCs.

1 Introduction

Hybrid organic-inorganic perovskite solar cells (PSCs) have gained extraordinary attention because of their high power conversion efficiency (PCE) and solution processability. Strong and wide optical absorption, high charge carrier mobilities, long carrier diffusion lengths, and surprisingly low recombination rates in hybrid perovskites have enabled PCE of 27 % in single-junction PSCs and about 35 % in silicon/perovskite tandem cells[1–4]. Furthermore, bandgap tunability and low-temperature fabrication techniques make PSCs potential alternatives to develop low-cost solar cells to compete with existing silicon photovoltaic technology.

A typical PSC consists of a transparent conducting oxide (TCO) as one of the electrodes, an electron transport layer (ETL), a perovskite absorver, a hole transport layer (HTL) and a top electrode. TCO is usually deposited on a glass substrate. The light enters from the Glass/TCO side. Top contact nomenclature comes from the fabrication scheme, as this is the last layer deposited on top of the underlying stack. A metal contact is commonly used as the top contact. Organic and inorganic wide-bandgap semiconducting materials are used as ETL and HTL. The absorber material, an arganic-inorganic hybrid perovskite consists of an ABX_3 type crystal structure. Where A is organic cation (such as Methylammonium, Formamidinium), B is an inorganic cation (such as Lead or Tin), and X represents the halogen anion (I, Br, Cl). Figure 1 shown a typical PSC structure, perovskite absorber crystal structure and energy diagram of a PSC. Upon sunlight exposure, electron-hole pairs are generated in the perovskite absorber. Due to the built-in potential developed by the means of different energy levels of absorber and transport layers, the electrons travel via ETL to the electron collecting electrode. The holes from the absorber valence band travel via HTL to the hole collecting elec-

[a] School of Energy Science and Engineering, Indian Institute of Technology Guwahati, Guwahati, Assam, 781039, India. E-mail: singhajay@iitg.ac.in
[b] Chair of Simulation of Nanosystems for Energy Conversion, Department of Electrical Engineering, TUM School of Computation, Information and Technology, Atomistic Modeling Center (AMC), Munich Data Science Institute (MDSI), Technical University of Munich, Hans-Piloty-Straße 1, 85748 Garching, Germany. E-mail: alessio.gagliardi@tum.de

View Article Online
DOI: 10.1039/D5EL00040H

trode.

Despite high efficiencies demonstrated by PSCs, several long-term and short-term instabilities hinder their commercialization and long-term deployment[7–9]. Photovoltaic performance of PSCs is hampered by grain boundaries (GBs), traps, and mobile ionic defects. The role of defects and charge transport in PSCs is a complex phenomenon and not very well understood. The organic-inorganic hybrid nature of the perovskite absorbers introduces complexity in understanding their electronic and optoelectronic behavior. This complexity is further amplified by the interplay of mobile ions, traps, grain boundaries, and introduction of interfaces at absorber, charge transport layer (CTL) and electrodes. PSCs exhibit hysteresis in the current-voltage (J-V) characteristics which is attributed to be a combined effect of traps, grain boundaries and mobile ions as confirmed by impedance spectroscopy[10–12], a combination of impedance spectroscopy and deep-level transient spectroscopy[13], wide-field photoluminescence imaging microscopy[14] and other techniques[15–17]. Ionic defects, grain boundaries, J-V hysteresis and instabilities in PSCs are regarded to be strongly interlinked, however, their correlation is not very well understood[11,18–20]. Because of mutual dependencies, experimental techniques often fall short in isolating the effects of individual parameters and physical processes such as ionic-electronic interaction, interface recombination, and grain boundary dynamics. Moreover, limitations in measurement techniques may limit the investigation and, hence, the understanding of various fundamental processes at the material and device levels. Simulation models, mainly by decoupling the effects of individual parameters, offer a complementary approach to investigate complex phenomena that would otherwise be difficult to understand using experiments.

Drift-diffusion (DD) is a promising tool to investigate underlying device physics, interface energetics and to optimize device architecture for obtaining maximum photovoltaic performance of PSCs[21–24]. DD modeling of PSCs has been implemented in several commercial and open course tools, such as, SCAPS-1D, Fluxim, OghmaNano, COMSOL, AFORS-HET, TCAD, AMPS-1D, TiberCAD, IonMonger, SIMsalabim and Driftfusion[25–35]. DD models have been employed to optimize material and device parameters, such as conductivity, doping, mobility, thickness and contact workfunction have been demonstrated using DD models[6,24,32,33,36]. Apart from device optimization, a significant effort has been dedicated to investigating J-V hysteresis[17,18,34,37,38] and the role of grain boundaries[16,27,39,40]. However, deeper investigations are required to get a clear picture of the contradictory role of grains[41–43]. The role of ferroelectricity in PSCs has been a topic of debate[44] with several DD models highlighting the importance of considering the role of ferroelectric domains in perovskite films[45–47]. Along with single-junction PSCs, DD models have been proposed to optimize material and device parameters in perovskite-based tandem solar cells[24,48–50]. Overall, the DD models have made a significant contribution to understanding various aspects of PSCs.

A basic DD model employs solving Poisson's and continuity equations simultaneously for all possible charged species in the system. The continuity equations include generation, recombination, and/or annihilation of charges. Considering only the electrons and holes to be generated upon light exposure, a simplified DD model for PSCs can be defined by the following set of equations[34,37]:

$$\begin{cases} \nabla\cdot(\varepsilon\nabla V) = -q\left(n-p+N_{\mathrm{a}}^{-}-N_{\mathrm{d}}^{+}-N_{\mathrm{ct}}+N_{\mathrm{an}}+n_{\mathrm{t}}^{-}-n_{\mathrm{t}}^{+}\right) \\ \nabla\cdot j_n = \nabla\cdot\{\mu_{\mathrm{n}} n\,(\nabla\Phi_{\mathrm{n}})\} = G-R \\ \nabla\cdot j_p = \nabla\cdot\left\{\mu_{\mathrm{p}} p\,(\nabla\Phi_{\mathrm{p}})\right\} = -(G-R) \\ \nabla\cdot j_{ct} = \nabla\cdot\left\{\mu_{\mathrm{ct}} N_{\mathrm{ct}}\left(k_{\mathrm{B}}T\,\frac{\partial N_{\mathrm{ct}}}{\partial x}\right)\right\} = 0 \\ \nabla\cdot j_{an} = \nabla\cdot\left\{\mu_{\mathrm{an}} N_{\mathrm{an}}\left(k_{\mathrm{B}}T\,\frac{\partial N_{\mathrm{an}}}{\partial x}\right)\right\} = 0 \end{cases} \tag{1}$$

Where the first row equation represents the Poisson equation consisting of all possible charge densities. Densities of electrons (n), holes (p), ionized donor (N_d^+) and ionized acceptor (N_a^-), electron trap (n_{t}^-) and hole trap (n_{t}^+) are considered. Mobile ionic defects are well-known in PSCs. For simplicity, two types of ionic defects are considered. Positively charged mobile ions are represented by cations with their density (N_{ct}), and negatively charged mobile ions are represented by anions with their density (N_{an}). The final four equations within the set of equation 1 are the continuity equations for the electrons, holes, cations, and anions. The negative sign in the hole continuity equation represents the opposite direction of the hole current as compared to the electrons when they both move in the same direction. Any additional charges (if present) must be included in the Poisson equation. Moreover, continuity equations must be defined for additional mobile charges. ε represents the material permittivity, V represents the electrostatic potential, and q represents the elementary charge.

μ_{p}, μ_{n}, μ_{ct} and μ_{an} represent the mobility of holes, electrons, cations, and anions, respectively. Φ_{n} denotes the electrochemical potentials of the electrons and Φ_{p} denotes the electrochemical potential of holes. All potentials and densities are a function of time and space. Assuming that the anions and cations are neither generated nor recombined, the right-hand side of the cation and anion continuity equations are set to zero. Further details on the numerical solver can be found in the references[34,37,51,52].

In PSCs, electrons and holes can recombine by different processes, leading to losses. R represents the net recombination rate governed by the sum of radiative and non-radiative recombination densities. Radiative or direct (bimolecular) recombination is defined as:

$$R_{\mathrm{dir}} = k_{\mathrm{dir}}\left(np - n_i^2\right)\,, \tag{2}$$

where k_{dir} is the bimolecular recombination rate coefficient. n_i represents the intrinsic carrier density. To include the effect of trapping of charge carriers by defects and the traps, Shockley-Read-Hall recombination is governed by[53,54]:

$$R_{\mathrm{SRH}} = \frac{np - n_i^2}{\left(n + N_{\mathrm{c}}\exp\left(\frac{E_{\mathrm{t}}-E_{\mathrm{c}}}{k_{\mathrm{B}}T}\right)\right)\tau_{\mathrm{p}} + \left(p + N_{\mathrm{v}}\exp\left(\frac{E_{\mathrm{v}}-E_{\mathrm{t}}}{k_{\mathrm{B}}T}\right)\right)\tau_{\mathrm{n}}}\,, \tag{3}$$

where E_{t}, E_{c} and E_{v} represent the trap energy level, the conduction band minimum and the valence band maximum. Note that a trap energy falling within the bandgap is considered. If the trap

View Article Online
DOI: 10.1039/D5EL00040H

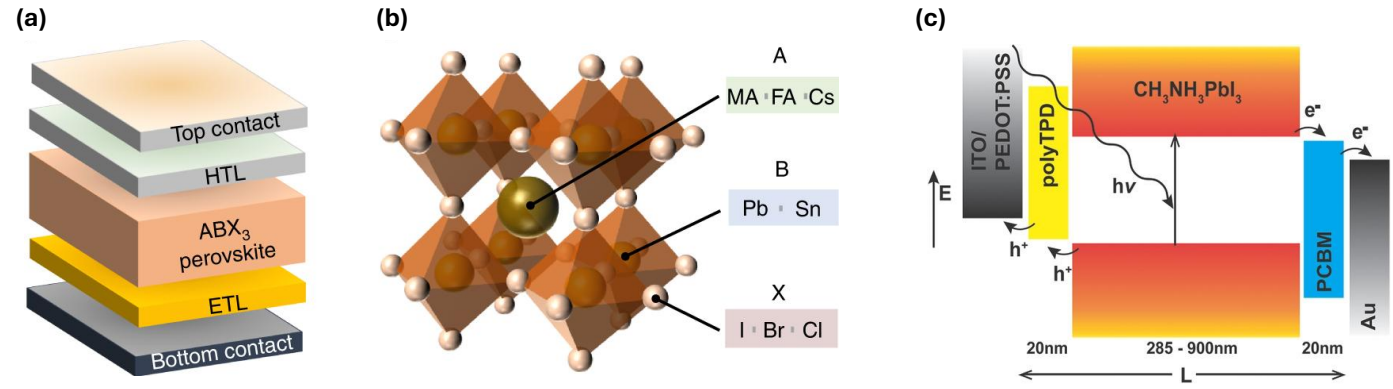

Fig. 1 (a) Typical perovskite solar cell structure. (b) ABX_3 crystal structure of perovskite absorbers. MA, FA and Cs stand for Methylammonium, Formamidinium, and Cesium, respectively. (C) Energy level diagram of a PSC consisting of ITO as TCO PolyTPD as HTL, $CH_3NH_3PbI_3$ as absorber PCBM at ETL and gold (Au) as top contact metal electrode. (a) and (b) are adapted with permission from ref[5], Copyright © 2022, Springer Nature. (c) is adapted with permission from ref[6]), Copyright 2017, John Wiley and Sons.

energy level lies within the conduction band or valence band, the charge carriers get detrapped and can move freely. N_c and N_v are the effective density of states within the conduction and valence band. τ_p and τ_n are the trapping times of holes and the electrons. The trapping time is defined as a function of capturing coefficient $C_{n,p}$ and the trap density as follows:

$$\tau_{n,p} = \frac{1}{N_t C_{n,p}} . \tag{4}$$

Higher $C_{n,p}$ and higher trap density (N_t) result in more efficient trapping and hence shorter trapping time $\tau_{n,p}$. In PSCs, recombination in the bulk perovskite films is usually low, which explains the long diffusion lengths of charge carriers and the higher efficiency of PSCs. Therefore, trapping times within the perovskite absorber are considered to be high. On the other hand, due to interface defects, smaller trapping times are considered at the ETL/perovskite and the perovskite/HTL interfaces. Any other recombination process present in the cell should be accounted for in the electron and hole continuity equations.

Upon light exposure, the electron-hole pairs are generated in the perovskite absorber, and the generation rate G is governed by a Lambert-Beer model for absorption:

$$G(x) = \int_{\lambda_{min}}^{\lambda_{max}} \varphi(\lambda)\,\alpha(\lambda)\exp(-\alpha(\lambda)x)\mathrm{d}\lambda , \tag{5}$$

where $G(x)$ is the generation rate at position x along the film thickness. $\varphi(\lambda)$ denotes the light intensity at given wavelength λ. α represents the absorption coefficient and can be determined experimentally via absorption measurements. Alternatively, $\alpha(\lambda)$ as a function of wavelength λ can be extracted by using the imaginary part of refractive index, κ, defined as[55,56]:

$$\alpha(\lambda) = \frac{4\pi\kappa}{\lambda} . \tag{6}$$

κ can be measured by optical measurements such as ellipsometry. The amount of available light within the perovskite absorber is determined by the optical properties of all the layers present in the device stack. The role of various layers can be captured by a Transfer Matrix Method, which is discussed in later sections.

To solve the Poisson's equation two boundary conditions are needed. The common approach is to use Dirichlet conditions (defined-variable value); the potential is fixed at both boundaries at each point is fixed at a given time, t. The electrostatic potential boundary conditions can be defined as[39]:

$$q(V_l - V(0) + V_{app}) = W_c - W_a \tag{7}$$

where, V_{app}, W_a and W_c represent the applied voltage, anode workfunction and cathode workfunction, respectively. For simplicity, potential of one of the contact can be set to zero as a reference[34]. The charge carrier density boundary conditions at the electrode contacts are governed as[39]:

$$n, c = N_{cv} exp(-\psi_{n,p}/V_t) \tag{8}$$

Where, $\psi_{n,p}$ denotes the offset (in eV) between the anode (cathode) workfunction and the valance (conduction) band of the perovskite. For the ions, blocking boundary conditions are used as the ions cannot come out of the perovskite layer. The ionic densities as well as the ionic currents are therefore set to zero at both ends of the device.

Most numerical DD models use a finite-element mesh (FEM) to define various layers and their properties in respective regions. During the simulations, a typical approach is to first calculate an equilibrium solution at short-circuit conditions without illumination. Thereafter, the illumination is switched on, and a steady-state solution is obtained. After reaching the steady state, a voltage sweep is applied to obtain the J-V characteristics of the device. A simplified one-dimensional model without considering ions and grain boundaries can be used to find steady-state J-V characteristics. Such simplified models can be handy to investigate the role of materials and device parameters optimize PSCs as presented by Sherkar *at al.*[6]. Figure 2 shows how the PSCs J-V performance can be optimized by varying charge carrier mobility (in absorber layer), injection barrier (defined by the electrode workfunctions and the charge transport layer conduction and valence bands), electron trap density, hole trap density, and doping in HTL.

View Article Online
DOI: 10.1039/D5EL00040H

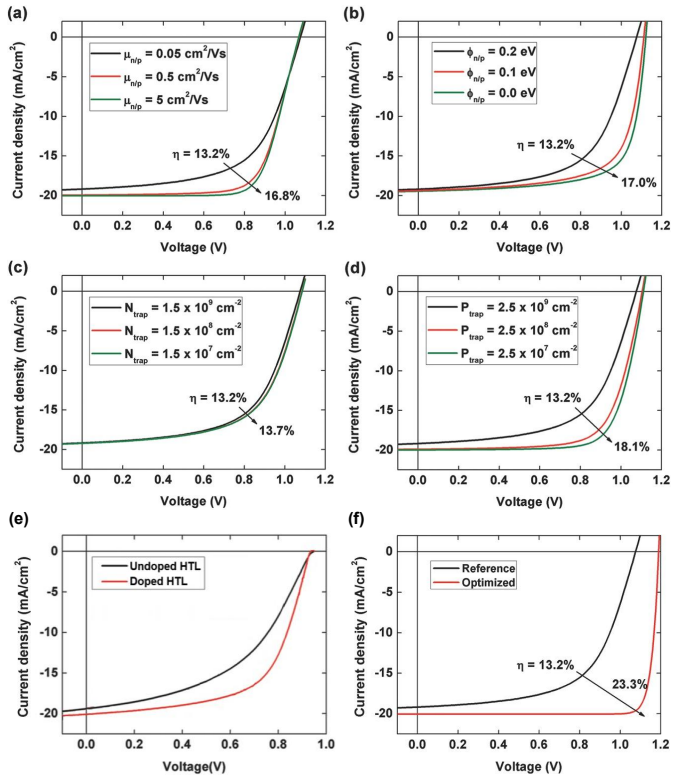

Fig. 2 Simulated J-V curves for different perovskite solar cells: (a) Charge carrier mobilities in perovskite absorber, (b) injection barriers, (c) electron trap density at ETL/perovskite interface, and d) hole trap density at perovskite/HTL interface. (e) the simulations with and with HTL doping. (f) Optimized device with increased carrier mobilities, reduced energetic barriers and, passivated traps. Reproduced with permission from Ref.[6] Copyright 2017, John Wiley and Sons.

Approximated steady-state DD models can represent the device performance trend under certain given conditions. However, the steady-state models cannot simulate J-V curves for different voltage sweep rates, and hence cannot give information on the J-V hysteresis. To get the information on the hysteresis, a forward bias (low to high voltage) is applied followed by a reverse bias (high to low voltage). Detailed discussion on J-V hysteresis is presented in later sections.

Many DD studies presented in the literature consider various approximations and hence may not represent the real device behavior despite reproducing J-V curves as pointed out by Neukom *et al.*[51]. Common approximations include geometry consideration, generation and recombination models, constant temperature approach, number and parameters of ionic defects, the role of grain boundaries and interfaces, etc. Tessler and Vaynzof have[57] highlighted the importance of including correct models and appropriate parameterization, especially for including the role of ions, dielectric constant, density of states, spatial distribution of recombination losses, etc. On the other hand, there has been little on modeling of the instabilities and hence the device performance in the long run. Minimizing the approximations, better parameterization and incorporation of appropriate submodels are needed to get the real picture of the performance of PSCs. This review critically examines various studies on DD modeling in PSCs to simulate transient and steady-state behavior, interface and grain boundary effects, ionic transport, and long-term stability. A comprehensive review of past studies and thier limitations have been presented. Thereafter, we have presented how future studies can adapt emerging strategies to improve the accuracy and predictive power of DD models, such as by implementing refined grain boundaries and interface models, machine learning- based acceleration, interfacing experimental data, and parameterization with the help of Density Functional Theory calculations. Moreover, we propose how inclusion of electronic-ionic interactions, and annihilation and creation of ionic defects can help predicting short- and long-term performance degradations in PSCs. By thoroughly reviewing current modeling approaches and proposing future pathways for refinement, this review aims to guide the development of robust and physically grounded DD models for PSCs.

2 Geometrical considerations

2.1 Interfaces and Grain Boundaries

Modeling the interfaces is one of the challenges in simulating PSCs. Most of the studies presented in the literature employ abrupt endings of material on both sides of the interface, which may not be true in a real device. The interfaces between the CTL and the perovskite absorber, and between the CTL and electrodes (cathode and anode) play crucial roles in the charge transport and recombinations at the respective interfaces. Some studies defined perovskite/CTL interface regions via 1 nm to 2 nm thick layers consisting of traps[39,51,58]. These studies consider the material properties in the interface region the same as the perovskite layer. In a real device, however, the interface can have a mixture of the perovskite and the particular transport layer. Therefore, a gradual variation of material properties would result in more realistic parameterization for the interface. Some studies have therefore employed a linear variation of material properties at the interfaces between perovskite and the CTL[37,52,59]. The same strategy could be applied to the interfaces between CTL and the electrodes. However, in-diffusion of (i) metal into the organic CTL, (ii) ionic defects into the CTL, and (iii) CTL dopants to the interface/bulk absorber, can make these interfaces even more complex to model[60,61]. Moreover, a change in built-in potential via the formation of self-induced dipoles can change the device performance[57].

Due to the polycrystalline nature of perovskite films, they consist of several grains oriented in different directions. The boundary between two adjacent grains may consist of dangling bonds, distorted bond angles, and other defects. Traps at the grain boundaries have been regarded to be one of the major loss mechanisms in PSC performance[19,41,42,62]. Apart from hosting fixed traps and recombination centers, GBs provide channels for ionic defect migration due to their low activation energies[41,63,64]. Therefore, the GBs play an important role in well-known J-V hysteresis in PSCs[11,41,64,65]. A summary of how various studies have modeled grain boundaries in PSCs is presented in table 1. Olyaeefar *et al.* proposed a classical model combined with a DD model to investigate the impact of grain size and boundary effects in

View Article Online
DOI: 10.1039/D5EL00040H

PSCs[27]. The model incorporated the impact of GBs by using equivalent mobility and carrier lifetimes within the perovskite layer itself. Similarly, Iftiquar *et al.* used an AFORS-HET-based one-dimensional DD model to simulate the impact of GBs by incorporating GBs equivalent of the volume defect density within the perovskite layer[66]. Sherkar *et al.* used a one-dimensional DD model to investigate the nature of ionic trap states within grain boundaries using fixed trap densities at the points 100 nm apart along the absorber thickness[39]. Nandal *et al.* investigated ion-induced passivation of grain boundaries using a DD model[67]. In the latter, the GBs are defined as 2 nm thick lines along with the length and perpendicular to the ETL/perovskite/HTL stack thickness. The GB properties were defined the same as perovskites except for a different trap-assisted recombination rate. The study observed that the orientation and location of GBs play an important role in the photovoltaic performance of PSCs. Moreover, GB to GB heterogeneity of adjacent grains can affect the photovoltage in PSCs[68]. Jia *et al.* pointed out the role of GB orientation by investigating the role of residual charges on photovoltaic performance[69]. The study demonstrated that the residual charge exists predominately at the grain boundaries which are parallel to the device. One of our studies implemented GBs as 1 nm to 2 nm thick regions oriented in different directions in a 2D plane[16]. We observed significant variations in photovoltaic performances with changes in the traps and ionic defect distribution profiles along with GBs. Considering all the aforementioned reports, it is important to correctly capture the size and orientation of the grain boundaries. In a real 3D bulk perovskite film, GBs are oriented in various directions and are distributed randomly. One-dimensional models fail to effectively and accurately mimic GB's orientation and distribution. Going beyond one-dimensional models is a necessity to fairly capture the role of GBs.

Another aspect of GBs is the presence of ordered ferroelectric domains associated with grains oriented in different directions. Rossi et al.[46] included the effect of polarization orientation pattern to simulate PSCs using a 2-dimensional DD model as shown in figure 3. The study implemented single-grain and multi-grain models using a trap density model associated with GB interfaces. The study highlighted the importance of the inclusion of ferroelectric domains-led polarization to reproduce the experimental J-V characteristics. The same group has presented another 3-dimensional DD model to investigate the role of ferroelectricity in PSCs[47]. Importantly, such 2-dimensional and 3-dimensional DD models can be extended to investigate the combined role of grain boundaries (such as defect states and ionic migration) and ferroelectricity.

Overall, accurate representation of grain boundaries, interfacial energetics and cocal variations is imperative for enhancing the predictive fidelity of DD simulations, as as these regions critically influence charge transport, recombination dynamics, and overall device performance in PSCs.

2.2 Mesoporous versus planar structure

Mesoporous scaffold-based PSCs offer higher surface area contacting the perovskite and charge transport layer; therefore resulting in improved charge extraction.[73,74]. A one-dimensional FEM cannot define mesoporous layers and therefore higher-order geometries are desired. Commercial 3D simulation packages combining finite-difference time-domain and FEM have been used to simulate PSCs[28,75,76]. However, most of these studies use planar architectures and make several approximations for the number of charged species and their interactions. In one of our studies, we presented a 2D mesh-based DD model to investigate the role of perovskite infiltration into mesoporous TiO_2[29]. The study gives a good approximation of the role of pore-filling and the interface defects, in agreement with the experimental findings as shown in Figure 4. To get a complete picture however, a 3D mesoporous FEM is desired.

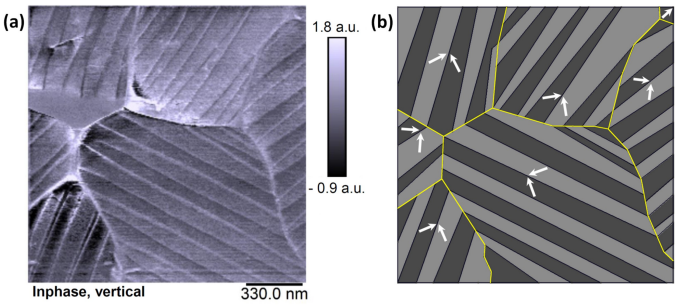

Fig. 3 (a) Piezo-response force micrographs and (b) the anticipated ferroelectric domain polarization used in the DD model as a representative of multi-grain surface section. Reproduced from Ref.[46], Copyright (2018), with permission from Elsevier.

2.3 Charge carrier generation profile and local variations in bandgap and defects

The charge carrier generation is determined by the amount of available light and the absorption coefficient of the absorber layer. Several studies consider constant or exponential decay charge carrier generation profiles obtained by the Lambert-Beer model for absorption while omitting the role of transport layers and contacts[17,38,58,77–79]. However, a real device undergoes reflection and parasitic absorption losses in CTL. The reflections and interface patterns from various layers can significantly change the optical profile and, hence the charge carrier generation in the absorber layer. The optical profile is determined by the thickness and optical constants (refractive index n_r, and extinction coefficient, k) of all the layers stacked together. Several studies simulate the role of metal contacts as just a fixed workfunction[17,78–81]. A PSC's back contact determines if the unabsorbed light will be transmitted or reflected back to the absorber. A reflection from a metal back contact permits more absorption in the absorber layer. This phenomenon can explain why opaque metal contact may result in higher current densities in comparison to semitransparent back contact while keeping the remaining layers unchanged[29]. To get right into the PSC's performance, a correct optical profile must be obtained. The transfer matrix method combined with the absorption models is a way to fairly include the optical role of the various layers and to fairly calculate charge carrier generation rates[6,59,82–85].

During the cell operation, the charge carriers undergo trapping

View Article Online
DOI: 10.1039/D5EL00040H

Table 1 An overview of grain boundary models used in drift-diffusion simulation of PSCs

Authors, year	GB Model	Reference
Olyaeefar *et al.*, 2018	Equivalent mobility and carrier lifetimes within perovskite layer	27
Iftiquar *et al.*,2018	Equivalent volume defect density within perovskite layer	66
Sherkar *et al.*, 2017	Fixed trap densities at certain points along the absorber thickness	39
Chu *et al.*, 2017	A thin slab sandwiched between two adjacent volumes in 3-dimensional model	70
An *et al.*, 2021	Effective charge carrier recombination rates in bulk perovskite film	62
Nandal *et al.*, 2019	2 nm lines along with the length and perpendicular to the charge flow in perovskite layer	67
Singh *et al.*, 2020	Distributed lines in various orientations in a 2-dimensional plane of perovskite layer	16
You *et al.*, 2021	Two-dimentional grooves in perovskite layers filled with HTL material	71
Kaiser *et al.*, 2022	Distributed points with different energy levels along the absorber thickness	40
Ali Hajjiah, 2025	Horizontal and vertical lines of different thicknesses in a 2-dimensional plane of perovskite layer	72

and/or recombination, which strongly depends on the available charge carrier density. At a given point, a higher charge carrier generation implies a higher recombination probability. The traps and recombination centers can be non-uniformly distributed throughout the device stack. Distribution of recombination centers combined with different carrier distribution can affect the photovoltaic performance[86]. If the regions with higher defects (such as interface traps) and high charge carrier generation coexist at the same point, there will be more trapping/recombination and vice-versa. Figure 5 elaborates on the scenario by considering simplified charge carrier generation profiles and recombination centers.

For simplicity, the effects of ETL, HTL and contact layers are ignored. Generation profile G1 (G2) is obtained if the cell is illuminated from the ETL (HTL) side. Values for the perovskite layer thickness and charge carrier generation rate are taken as typical values for PSCs based on the literature. As an example, in the case of G1 (maximum value chosen based on references[6,16,52]), electron traps near the ETL/perovskite interface will experience $1 \times 10^{22}\,\mathrm{cm}^{-3}$ electrons. If the light is incident from the HTL side, the same electron traps will experience $1 \times 10^{20}\,\mathrm{cm}^{-3}$ electrons for a possible trapping/recombination. Therefore, the recombination losses will be higher in the case of the illumination from the ETL side. Similarly, hole traps will affect the device's performance based on their position and the light illumination side in the cell. The charge carrier profile and, hence the trapping/recombination will be modified by the light reflection and interference patterns while considering the optical effect of CTL and the contacts. Our recent study explains why illuminating from the TiO_2 (ETL) side results in a different loss mechanism than illuminating from the opposite side[87]. This can also explain why p-i-n and n-i-p structures have different charge transport mechanisms given the same absorber quality[88,89].

Furthermore, local variation in bandgap can modify light absorption and hence charge carrier generation and their recombination profiles; ultimately, the photovoltaic performance[90,91]. Also, a difference in the bulk and surface workfunction can modify the charge extraction and hence the photovoltaic performance. Canil *et al.* observed a significant change in the photovoltaic performance upon tuning the surface workfunction of the perovskite layer[58]. Overall, considering appropriate optical models and the right spatial distribution of bandgap, traps and other properties is needed to obtain accurate and reliable results in a DD model.

2.4 Barrier layers and tunnelling effect

Various architectures employ thin barrier layers to block ionic transport to the CTL. Surface passivation using 2D MXenes, 2D perovskites, and via dipole interlayer are well-known practices in high-efficiency state-of-the-art PSCs[90,92,93,93]. On the other hand, self-assembled monolayers as hole transport layers have gained great attention in recent years[94]. Most existing DD studies consider the passivating layer properties similar to the bulk perovskite layer itself. Our simulations for the effect of interface workfunction tuning found tuning of photovoltaic performance correlating to the experimental values[58]. In the study, we approximated the functionalized surface as a 2 nm layer similar to the bulk perovskite except for a different workfunction. For simplicity, we ignored the effect of quantum transports and considered abrupt junctions between various layers. To fairly include the effect of 2D passivating layer and self-assembled monolayers, quantum models should be adopted to account for the energy-level modification and tunnelling-dependent charge transport. For example, various p-i-n devices employ a thin BCP (bathocuproine) layer, which in principle can act as a tunnelling layer for electrons and a blocking layer for holes[95,96]. Depending on the thickness, the BCP layer leads to an improved fill factor or an "S" shape in the J-V characteristics. Considering only the blocking nature of this layer may result in misleading results[79,97]. In a thin layer, Fermi-level pinning moderates charge transport despite huge energy barriers presented by the balance and conduction band energies. Tian *et al.* presented a combined drift-diffusion and quantum transport for n-type TOPCon silicon solar cell[98]. The study found significant differences in the photovoltaic performance with and without considering the quantum transports. Similarly, to draw a complete picture of charge transport in PSCs via various layers and interfaces, quantum models in combination with the DD model are needed.

3 Ionic transport and J-V hysteresis

Weak metal-halide bonds within the halide perovskites (ABX_3) form a soft lattice prone to dynamic structural disorders and defects in the crystal[9,99–101]. The softness of the crystal makes halide perovskites unstable against temperature variations[101]. Several charged ionic defects such as interstitials and vacancies of halide anion, metal cation and organic cation can freely move within the perovskite absorber[13,99,102–104]. Ionic defect migration has been considered to be the main reason behind J-V hysteresis (forward bias and reverse bias scan do not follow each

View Article Online
DOI: 10.1039/D5EL00040H

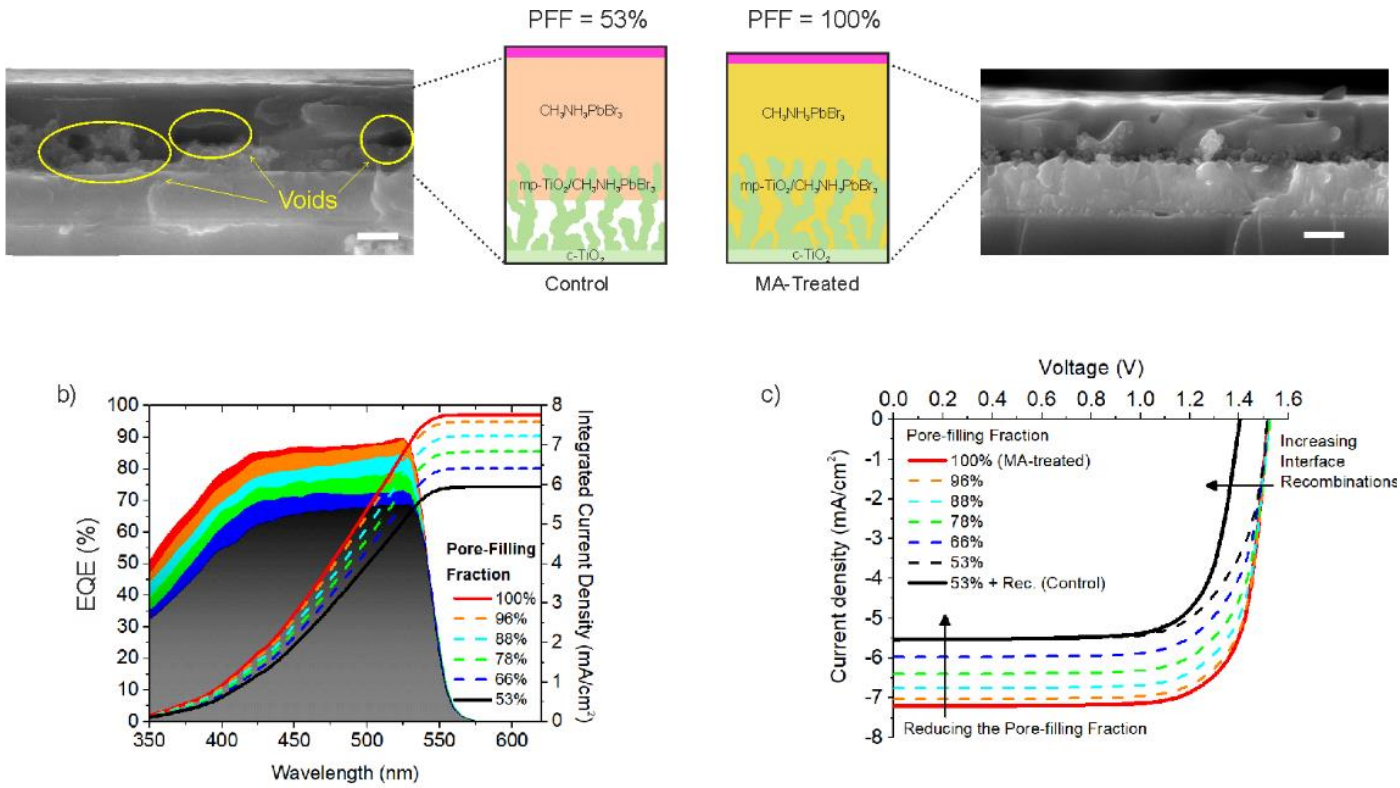

Fig. 4 2-dimensional DD model corroborating the experimental findings on pore-filling of perovskite into mesoporous TiO_2. (a) SEM images and DD model input geometry for pore filling factor (PFF). (b) Calculated external quantum efficiency (EQE) and integrated current density. (c) Calculated J-V characteristics with different pore filling and interface trap densities. The traps are considered at the mesoporous TiO_2/perovskite interface. The cell stack consists of FTO/compact-TiO_2/mesoporous-TiO_2/$CH_3NH_3PbBr_3$/PTAA/Gold. Reproduced with permission from Ref.[29], Copyright 2021, John Wiley and Sons.

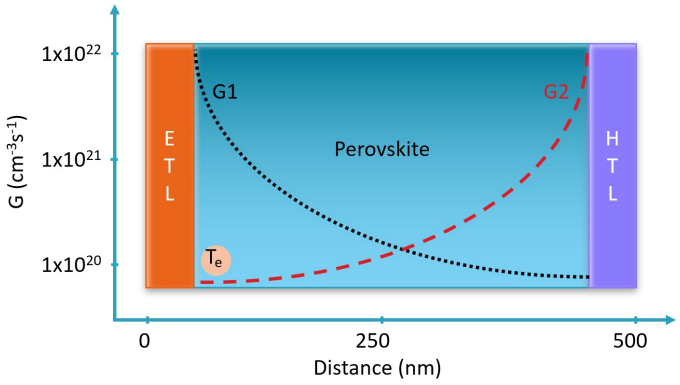

Fig. 5 Charge carrier generation profiles and electron traps in a perovskite solar cell. T_e represents an electron trap near the perovskite/ETL interface. G1 and G2 represent generation profiles upon light irradiance from the ETL and HTL sides, respectively.

other) in PSCs[11,15,17,37,105]. Ions can passivate GBs depending upon the polarity of ions and the location of GBs[67] and modulate the photovoltaic performance[106,107]. Moreover, chemical reactions driven by the ionic defects (such as iodine ions) can lead to non-reversible degradation of perovskite absorber[107]. Modeling the mobile ions' movement is one of the most complex processes to implement within DD models. This is mainly because of the lack of experimental values for parameters such as the type of ionic defects, their densities, distribution profiles, mobilities, diffusion coefficients, and preferred migration channels. Upon illumination, the photo-enhanced ion conductivity makes it even more complex to determine adequate parameters for ions[108]

Most of the DD studies consider one positive and one negative ionic species to investigate the impact of ions on the photovoltaic performance[18,38,51,52,109]. In a real device however, different ionic defects can result in more than two types of mobile ions moving with different properties including densities, mobilities, end associated energy levels. Considering more than two ionic species can pinpoint which species are responsible for certain characteristics. For example, certain mobile ions with a given density and mobility may not result in J-V hysteresis, while others can contribute to the same.

Not only the types and densities of ionic defects are under debate, but their distribution and migration channels are also. The densities and distribution of ionic defects play a crucial role in determining steady-state photovoltaic performance[16,67]. Some studies have suggested that the ionic defects move through the grain boundaries due to the lower activation energies at the GBs than the bulk of the grains[63–65]. One-dimensional DD models fail to capture simultaneously the GBs and the ionic movements via them, and therefore several approximations are considered. Table 2 summarizes some of the key DD studies that have investigated the role of various ionic defects in PSCs, considering their

View Article Online
DOI: 10.1039/D5EL00040H

different types, densities, and distribution profiles. Sherkar *et al.* considered fixed trap density to mimic ionic defects in their 1D simulations to investigate the nature of ionic trap states within grain boundaries[39]. Gagliardi *et al.* defined fixed electrostatic potential within mesoporous TiO_2 layer to mimic ionic distribution[110]. Canil *et al.* modeled steady-state photovoltaic performance by considering ions distributed within 2 nm interface layers between the perovskite and CTL[58]. Some studies considered the uniform ionic distribution within the perovskite layer[37,38,51,59]. Overall, the combined role of ionic defects and grain boundaries in photovoltaic performance is not very well understood. To get the real picture, a two or three-dimensional (both transient and steady-state) model consisting of GBs and multiple ionic species is desired.

Another important aspect to consider while modeling the impact of ions is their interactions with electrons and holes. Le Corre[36] modeled transient behavior by neglecting the effect of ions and SRH recombination, assuming that the ions do not move significantly at the microsecond timescale. In the model, including traps and SRH recombination or fixed ions resulted in identical outcomes as when only bimolecular recombination was considered. To note that the scenario when only bimolecular recombination is similar to the open-circuit condition when the cell delivers no power. In a real solar cell, it is (almost) impossible to avoid non-radiative recombinations. Neukom *et al.* modeled the steady-state and transient behavior while considering no interaction of the ions with electrons, holes and traps[51]. Calado *et al.* implemented a one-dimensional time-dependent DD model to study the role of ionic migration on the J-V hysteresis[52,59]. In their model, ions were considered to only screen the built-in potential, while trapping of charge carriers is neglected. However, several studies have pointed out the trapping nature of the accumulated iodine vacancies at GBs and interfaces[114–116]. Trapping by ionic defects might be one of the essential factors in the J-V hysteresis, as modeling without traps can result in hysteresis-free J-V profiles[6,37,52,111]. In a joint experimental-theoretical study by Domanski *et al.*, DD model included the recombination of electrons at mobile anions to investigate the transient behavior of the photocurrent[112]. This study was the first (to our knowledge) to analyze electrons' recombination at anions using a simplified bimolecular recombination model. Our previous study included electron trapping (and electron-hole recombination) at the mobile cation sites[37]. The study found that "ions-led built-in field screening only" leads to very low hysteresis than the experimentally observed values. Adding cation-mediated electron-hole recombinations results in hysteresis values similar to those experimentally observed. To our knowledge, trapping phenomena led by the anions have not yet been studied. Figure 6 shows calculated J-V profiles for various cases, i.e., with and without ions, with ions and traps, and, with ions, traps and cation-mediated recombination. Considering various possible trapping and recombination processes, it is still difficult to pinpoint the exact mechanism leading to the J-V hysteresis. Possibly, multiple phenomena contribute to the effect, and it is hard to experimentally measure independent contributions of various processes. DD models can help decoupling the contributions of various phenomena responsible for the hysteresis. However, the material and device parameterization is not coherent throughout the proposed studies. Therefore, appropriate parameterization on types and the number (could be more than just two) of ionic species, and their energy levels, densities, mobilities, migration channels, and interactions with charge carriers is necessary to draw a fair conclusion on the complex role of ionic defects.

4 Mobility models

Several DD models employ constant mobility models in perovskite absorber and CTL. In hybrid perovskite films, charge carriers and ionic defect mobilities depend on various factors, such as film stoichiometry, self-doping, energetic disorder, grain size, and ionic defect scatterings[117–120]. Moreover, during the operating conditions, temperature variations, degradation and other factors may lead to changes in charge carrier and ionic defect mobilities. More studies are needed to investigate the behavior of charge carriers and ionic mobility within the perovskite absorbers. On the other hand, charge carrier mobilities in transport layers depend on temperature, doping and electric field[121]. Therefore, modeling PSCs with constant mobility models may result in misinterpreting the calculated data. The inclusion of factors such as doping and temperature dependence is very important while modeling PSCs.

4.1 Temperature-dependent mobility

In a semiconductor crystal, lattice/phonon scattering and ionized impurity scattering affect the charge carrier mobilities[122,123]. Both the lattice scattering and ionized impurity scattering depend on the operating temperature. A generalized temperature-dependent mobility can be defined as:

$$\mu_T = \mu_0 \left(\frac{T}{T_0}\right)^m, \tag{9}$$

where, $T = 300\ K$ is the reference temperature. m is a constant governed by the scattering mechanisms in the material. The inelastic scattering of optical phonons results in a power law of $\mu \propto T^{-1/2}$, and the elastic scattering of acoustic phonons results in a power law of $\mu \propto T^{-3/2}$. Charge carrier scattering of ionic defects and impurities result in a power law of $\mu \propto T^{+3/2}$. In a hybrid perovskite film, mobility (for both the charge carriers and ionic defects) depends on various factors, such as film stoichiometry, self-doping, energetic disorder, grain size, and ionic defect scatterings[117–120]. Therefore, a mixture of various effects can lead to a different power law dependence. Biewald *et al.*[124] obtained a power law dependence of $\mu \propto T^m$ with $m = -(1.8 \pm 0.1)$ for MAPI perovskite. A theoretical study by Mayers *et al.* proposed a power law dependence of $\mu \propto T^{-2.11}$[125]. Savenije *et al.* proposed band-like dependence of mobility with $\mu \propto T^{-1.6}$[126]. Moreover, hybrid perovskite may undergo a phase change and the charge carrier mobility can differ in different crystalline phases[124].

4.2 Doping dependent mobility

In PSCs, CTL are doped to efficiently extract the charges from the absorber to the electrodes. Both organic and inorganic CTL have been used in perovskite solar cells[127,128]. In widely used organic

View Article Online
DOI: 10.1039/D5EL00040H

Table 2 Various drift-diffusion modeling studies on investigating J-V hysteresis and the role of ionic defects in PSCs

Authors, year	Ionic density	Ionic distribution	Remarks and findings	Reference
Reenen *et al.*, 2015	1×10^{15} cm^{-3}–1×10^{19} cm^{-3}	Free to move within perovskite layer	J-V Hysteresis is combined effect of mobile ions and traps. No hysteresis without traps.	111
Richardson *et al.*, 2016	1×10^{17} and 1.6×10^{19} cm^{-3}	Free to move within perovskite layer	Slow moving ions lead to the J-V hysteresis.	17
Calado *et al.*, 2016	1×10^{15} cm^{-3}	Distributed within perovskite layer	Combination of mobile ions and recombination centres leads to J-V hysteresis	52
Sherkhar *et al.*, 2017	1×10^{15} cm^{-3}	Distributed within perovskite layer and at the GBs	Ions can fill grain boundary traps and change the J-V hysteresis profile.	39
Gagliardi *et al.*, 2017	1×10^{16} cm^{-3}–1×10^{19} cm^{-3}	Distributed at the perovskite/TiO_2 mesoporous interface	Increased surface area dilutes the effect of ion accumulation.	110
Domanski *et al.*, 2017	1×10^{17} cm^{-3}	Distributed within perovskite layer	Trapping of electrons at mobile cations may lead to reversible performance losses.	112
Canil *et al.*, 2019	1×10^{17} cm^{-3}	Fixed charge density at perovskite interfaces	Ion accumulation at interface affects the steady-state performance.	58
Neukom *et al.*, 2019	5×10^{17} cm^{-3}	Distributed within perovskite layer	Charge injection is affected by ion accumulation at perovskite interfaces.	51
Nandal *et al.*, 2019	1×10^{17} cm^{-3} and 1×10^{18} cm^{-3}	Distributed at the grain boundaries	Ions can passivate the effect of grain boundary losses.	67
Singh *et al.*, 2020	1×10^{16} cm^{-3}–1×10^{19} cm^{-3}	Fixed in the bulk, at the grain boundaries and at the perovskite interfaces	Steady-state performance changes with ionic distribution.	16
Singh *et al.*, 2021	1×10^{18} cm^{-3}	Free to move within perovskite layer	Cation-assisted recombination enhances J-V hysteresis to experimentally observed values. Nominal J-V hysteresis without cation assisted recombanation.	37
Calado *et al.*, 2021	0 cm^{-3}–1×10^{19} cm^{-3}	Distributed within perovskite layer	Ionic redistribution screens the electric field and determines the steady-state performance.	59
Zhou *et al.*, 2021	5×10^{17} cm^{-3}	Distributed within perovskite layer	Dielectric constant of charge transport layers affects the hysteresis.	59
Minbashi *et al.*, 2022	9×10^{16} cm^{-3}	Distributed within perovskite layer	Inverted hysteresis is obtained when ions accumulate at the perovskite boundaries.	109
Almora *et al.*, 2024	1×10^{15} cm^{-3}–1×10^{18} cm^{-3}	Distributed within perovskite layer	Different recombination mechanisms are present at different ionic densities.	113
Wang *et al.*, 2024	1×10^{16} cm^{-3}–1×10^{18} cm^{-3}	Distributed within perovskite layer	J-V hysteresis is linked to device degradation.	18

CTL (such as Spiro-OMeTAD, Spiro-TTP, PolyTPD, PEDOT:PSS, C60, BCP, PCBM, PTAA, etc.), the charge carrier mobility is a complex function of the host-dopant interactions. Several groups have investigated doping-dependent mobility in various organic semiconductors [129–132]. Arkhipov *et al.* presented an analytical model to calculate charge carrier mobility in weakly and heavily doped organic semiconductors [133,134]. Koopmans and coworkers studied the electrical conductivity of fullerene derivatives [135]. Doping-dependent charge carrier mobilities for inorganic semiconductors can be found using empirical models similar to the ones proposed for silicon [136,137]. Along with the CTL, intentional or self-doping in the hybrid perovskites can lead to change charge carrier mobilities in the absorber layer [117,119,138].

Overall, to fairly capture the role of varying mobilities, appropriate temperature- and doping-dependent mobility models should be employed.

5 Stability

5.1 Ionic defects and grain boundaries driven instabilities

One of the major concerns hampering the commercialization of PSCs is their poor stability. Intrinsic factors such as ionic defects, surface and interface defects, grain boundaries, nanoscale phase impurities, and inhomogeneities have been reported to affect the short-term and long-term stabilities of PSCs [91,139–141]. Moreover, extrinsic factors such as exposure to light, temperature, and moisture affect the operational stability of PSCs. Nandal and Nair presented a modeling of ionic-migration-induced performance degradation in PSCs [142]. The origin of ionic defects can be both the intrinsic and extrinsic factors involving chemical processes leading to the creation and annihilation of ionic/neutral species [143–145]. Bitton and Tessler combined the DD model with iodine chemistry to investigate the annihilation of electrons and holes [107]. The study points out that certain chemical reactions can lead to mobile ionics defects and, hence, deterioration of the photovoltaic performance during the cell operation. The study considered only radiative recombination losses and the SRH recombinations were ignored. Theoretically, a negative ionic defect can capture a hole to become electrically neutral or can remain negatively charged via facilitating electron-hole recombinations. Similarly, a positive ionic defect may facilitate electron-hole recombination by capturing an electron. In the case of cation-assisted and anion-assisted recombination of electrons and holes, the electron and hole continuity equations should be updated with additional recombination processes. The updated electron and hole continuity equation can be written as:

View Article Online
DOI: 10.1039/D5EL00040H

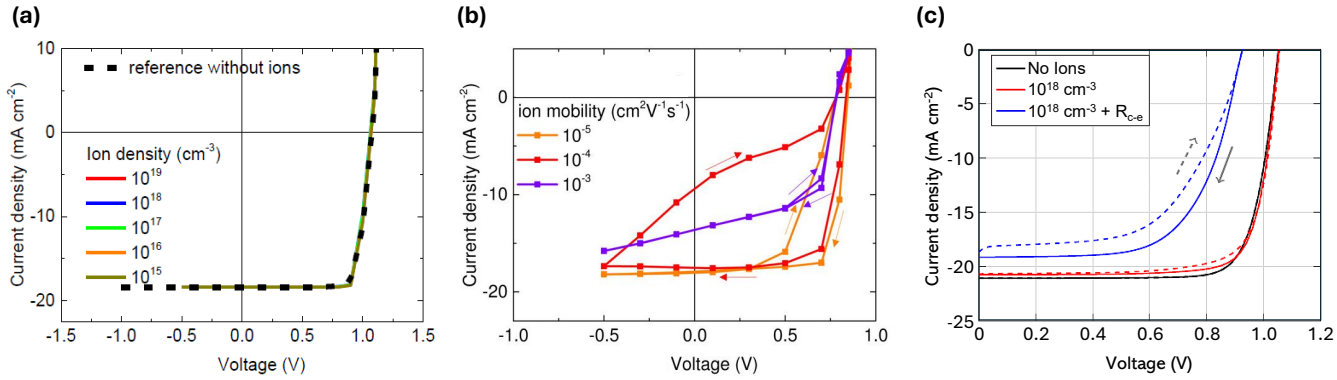

Fig. 6 Calculated JV characteristics for PSCs resembling FTO/TiO_2/$CH_3NH_3PbI_3$/Spiro-OMeTAD/Gold devices with: (a) comprising ions and no traps, (b) comprising ions and traps, and (C) comprising no ions, comprising ions and cation-assisted recombination. Red and blue curves in (c) correspond to ion density 10^{18} cm^{-3}. $R_{c\text{-}e}$ represents the presence of cation-assisted recombination. Both the anions and cations densities were kept the same to maintain charge neutrality. The arrows denote the sweep direction. Subfigures (a) and (b) have been adapted with permission from Ref. [111], Copyright 2015 American Chemical Society. Subfigure (c) has been adapted with permission from Ref. [37], Copyright 2021, Elsevier B.V.

$$\begin{cases} \nabla \cdot \{\mu_n n (\nabla \Phi_n)\} = G - R - R_{ct} - R_{an} \\ \nabla \cdot \{\mu_p p (\nabla \Phi_p)\} = R + R_{ct} + R_{an} - G \end{cases} \quad (10)$$

Where, R_{ct} and R_{an} represent the net electron-hole recombination rates led by cations and anions, respectively. The ions-assisted recombination rates can be modeled as defined in reference [37].

Creation and annihilation of new charged species will lead to disrupt the perovskite absorber crystal and hence drop in photovoltaic performance. DD model can help predicting photovoltaic performance losses by accounting for the new charged species. If new charged species are created and annihiliated (without involving free electrons and holes), additional continuity equations need be defined for each charged species. The continuity equations for the newly created/generated cations and anions in equation1 can be defined as:

$$\begin{cases} \nabla \cdot \left\{ \mu_{ct,new} N_{ct,new} \left(k_B T \frac{\partial N_{ct,new}}{\partial x} \right) \right\} = G_{ct,new} - R_{ct,new} \\ \nabla \cdot \left\{ \mu_{an,new} N_{an,new} \left(k_B T \frac{\partial N_{an,new}}{\partial x} \right) \right\} = R_{an,new} - G_{an,new} \end{cases} \quad (11)$$

Where, $G_{ct,new}$, $R_{ct,new}$, $G_{an,new}$ and $R_{an,new}$ represent the rates of creation of new cations, annihilation of new cations, creation of new anions, and the annihilation of new anions, respectively. To note that the continuity equations for new charged species (ct,new and an,new) will be there in addition to the existing continuity equations as defined in equation 1 (electrons, holes, existing cations and existing anions). At the same time, the Poisson equation (defined in equation 1) should be modified by including new charged species as following:

$$\begin{cases} \nabla \cdot (\varepsilon \nabla \Psi) = \\ -q \left(n - p + N_a^- - N_d^+ - N_{ct} + N_{an} + n_t^- - n_t^+ - N_{ct,new} + N_{an,new} \right) \end{cases} \quad (12)$$

Overall, by including the creation of electrically charged and neutral species and the ionic-assisted recombination processes can help predicting instantaneous as well as long-term fluctuations in photovoltaic performance.

Many DD models presented in the literature ignore the GBs-assisted degradation in PSCs. By visualizing the spatial evolution of local photoconductivity, Chu and co-workers reported that the degradation process is triggered by the disintegration of grains rather than nucleation and propagation from the visible grain boundaries [70]. This leads to the evolution of the shape and size of GBs over time. This GBs-led change in the distribution of defects and ionic species will change photovoltaic performance [16]. Moreover, spontaneous grain coalescence in the dark can enable the reduction of grain GBs-led photovoltaic losses [65]. By accounting for grain boundaries and evolved concentrations of static and mobile defects at GBs, DD models will help to investigate the role of GBs' evolution in the short-term and long-term performance of PSCs.

5.2 Thermal instabilities

Hybrid perovskites are shown to degrade under high temperatures and can be mediated via chemical reactions. The temperature influences the rate of chemical reactions and, hence, the rate of annihilation and creation of ionic defects. Variations in the ionic defect density and distribution change the ionic-electronic interactions and built-in field screening, and hence, the solutions to the Poisson and continuity equations. Moreover, the charge carrier (electronic-electronic) trapping and recombination times depend on temperature, defined as [146]:

$$\tau_n = \tau_n^0 \left(\frac{T}{T_0} \right)^{\alpha_n} e^{\beta \left(\frac{T}{T_0} - 1 \right)}. \quad (13)$$

Thermal variations also influence the charge carrier and ionic defect mobilities as discussed in previous sections. Furthermore, a temperature change can change the bandgap of a semiconductor, especially the absorber layer. The temperature-dependent material bandgap is defined as the following [147]:

$$E_g(T) = E_g(0) - \frac{\alpha_1 T^2}{T + \beta_1} \quad (14)$$

View Article Online
DOI: 10.1039/D5EL00040H

where, $E_g(0)$, α_1 and β_1 are material constants. The change in bandgap leads to a change in equilibrium charge carrier concentrations, defined as:

$$n = N_c\ exp\left(\frac{E_{fn}-E_c}{k_BT}\right) \quad \text{and} \quad p = N_v\ exp\left(\frac{-E_v+E_{fp}}{k_BT}\right), \quad (15)$$

where, N_c the N_v are the temperature-dependent effective density of states of the conduction and the valence bands, respectively, defined as [123]:

$$N_c = 2\left(\frac{2\pi m_e^* k_B T}{h^2}\right)^{\frac{3}{2}} \quad \text{and} \quad N_v = 2\left(\frac{2\pi m_h^* k_B T}{h^2}\right)^{\frac{3}{2}} \quad (16)$$

.

Similarly, the position of the Fermi level in doped semiconductors (i.e., the electron and hole transport layers) strongly depends on the operating temperature [123]. Therefore, during the cell operation, the temperature-dependent charge carrier concentrations should be updated in the continuity as well as the Poisson equations. Along with carrier concentrations, the temperature change can induce change in charge carriers' and ionic mobilities as explained in an earlier section. Overall, the temperature variation can change the concentrations, mobilities, and interaction patterns of various charged species within a PSC. To accurately consider the temperature dependence (especially while modeling the time-dependent performance evolution), the ionic defects creation and annihilation rates, carrier densities, mobilities, and their interaction should be implemented in appropriate equations.

6 Further Improvements

6.1 Inclusion of optical models and photon recycling

Optical modeling within DD governs the the light absorption and the spatial distribution of photogenerated carriers, which directly influences recombination dynamics and device efficiency. Transfer matrix Method in conjunction with Lambert Beers model nicely defines optical generation rate in a homogeneous absorber with no bandgap variations. Hetero interface-driven instabilities can however lead to bandgap variation and hence change in the light absorption (hence the charge carrier generation) profile locally [90,91]. Optical models accounting for local variation are desired in such cases. In high-efficiency devices where the defect-assisted non-radiative losses are nominal, radiative losses become the dominant loss mechanism. When the cell is producing non-zero output power, radiative recombination of electrons and holes result in photons that can be absorbed in different regions of the absorber layer. This phenomenon is commonly known as photon recycling. In the case of bandgap inhomogeneities and graded bandgap structures, photon recycling becomes even more prominent as the photon emitted by the high bandgap region can be absorbed by a low bandgap region. Incorporating photon recycling models within the DD can help improve the accuracy of the calculated data similar to the one reported in GaAs solar cells [148] and all-perovskite tandem solar cells [149]. Zedar *et al.* have demonstrated a coupled photon-recycling DD model for PSCs [150]. The model incorporated Green's function formalism with a charge-carrier DD model to account for reabsorption of internally emitted light. Improvement in both V_{oc} and PCE was observed upon inclusion of photon recycling. Brenes *et al* presented a combined experimental and detailed balanced model to calculate the effect of photon recycling on PSC's J-V performance [151]. Upon accounting for the effect of light scattering in a photon recycling model, the study found increase (77mv) increment in V_{OC}. The study however does not account for local variation in bandgap and non-radiative near-field coupling to the nearby perovskite. However, both the studies point out the underestimation of photovoltaic performance while simulating PSCs while ignoring the photon recycling. Inclusion of in bangap inhomogeneities and photon recycling in DD models remains largly explored. Thereby, the studies integrating wavelength (bandgap)-resolved optical models and photon recycling mechanisms into DD frameworks are critical for accurately capturing the local and global carrier generation and recombination in PSCs.

6.2 Time/frequency dependence

Steady-state DD modeling cannot capture the effect of several kinetic phenomena occurring in PSCs at short time scales, especially those linked to ionic defects. Since the ions remain within the perovskite layer itself and cannot be transported to the external contacts, accurately capturing their interactions becomes very important. To capture such phenomena, time- and frequency domain analysis are needed for the stacks with and without charge transport layers. Incorporating light intensity-dependent open-circuit voltage and photocurrent, capacitance-voltage, transient photocurrent and voltage-step responses give deeper insights into various phenomena not captured by simple DD models [21]. Bou *et al.* [152] have pointed out the importance of combining drift-diffusion and frequency dependence analysis to reproduce experimentally observed data in PSCs. Balaguera *et al.* implemented time-dependent capacitive current equations to calculate how the PSC performance evolves with J-V scan frequency [153]. The capacitive behavior is governed by the geometrical capacitance as well as the movements of ions and charge carriers. The study goes beyond simple DD equations and captures kinetic processes linked to the ions and J-V hysteresis. As reported by Riequelem and co-workers, combining impedance spectroscopy (IS) with DD model can reveal the underlying device physics and mechanisms responsible for recombination losses and charge collection efficiency in PSCs [154]. By investigating high-frequency IS spectra and DD calculations, the study suggested that the steady-state performance governed by is the distribution of mobile ions within the perovskite absorber layer. Nuekon *et al.* [51] presented steady-state, transient, and frequency-domain analysis for PSCs by using Setfos 4.6 from Fluxim. Using transient current analysis under dark conditions (applied voltage), the steady revealed interface recombination process modulated by the accumulation of mobile ions. The study however failed to explain a raise in delayed current while reversing bias (+3V to -3V). The study speculated mobile ions driven chemical reactions to cause the effect. Clarke *et al.* [155] implemented time-dependent degradation factor to the recombi-

View Article Online
DOI: 10.1039/D5EL00040H

nation rate in modified DD software IonMonger. By combining current–voltage and impedance measurements, the study pointed out the possibility of charge carriers and the ion vacancies in perovskite layer. Almora *et al.* proposed a short-circuit IS combined with DD modeling to investigate instability in PSCs. The study found that the ionic conduction is led by different pathways for at different mobile ion concentrations.

Clarke *et al.*[21] employed approximated DD model to explain multi-feature Nyquist plot for PSCs. The model pointed out the possibility of creation of a small population of 'excess ionic defects' at DC voltage, leading to neutralise electronic charges in the bulk perovskite layer at a different time scale than the ionic movements. The mid-frequency spectra suggests ion-modulated recombination rate in the perovskite bulk. Both the observations are helpful in understanding the role of creation of new ionic defects and electronic-ionic interactions leading to J-V hysteresis and instability in PSCs. More of such studies at different time/frequency scales will help in drawing a clear picture on the underlying phenomena responsible for short- and long term instabilities in photovoltaic performance of PSCs.

6.3 Combining Density-Functional Theory and DD

DD needs various input parameters to perform charge transport calculations. Some of the parameters can be obtained from experiments. However, changing the environment (i.e., employing multilayers, using thin passivating layers, interface modifications, microscopic inhomogeneities, etc.) can alter the parameter's values while fabricating a complete device. Moreover, fabrication conditions (deposition methods, temperature, humidity and oxygen levels, post-deposition processing, storage, etc.) are crucial in determining electronic, optical and optoelectronic properties of different layers. Density-functional theory (DFT) is a well-known and versatile method to calculate (but not limited to) physical, thermal, mechanical, electronic, optical and optoelectronic properties of materials[156,157]. In PSCs, DFT can help in incorporating the roles of crystal structures, spin-orbit coupling, bandgap tuning by substitution/mixing, dielectric constant, photoabsorption coefficient, phonons and material stability, defect formation, ion diffusion, and surfaces and interfaces[158]. DFT has been independently used to calculate material properties[159–161], investigating ionic defects[159,162], and investigating interfaces and other components of PSCs[58,90,163]. Still, several phenomena taking place within a perovskite solar cell (especially at the atomistic level in ABX_3 perovskites and at the interfaces) are not very well understood and hence are not captured while simulating PSCs. Combining DFT and DD offers a way to simulate a PSC from material to device levels.[164] Marimuthu el al. presented a combined experimental, DFT and DD study to investigate the possibility to use dimethyl ammonium metal formate-based crystals $[(CH_3)2NH_2]Co_{1-n}M_n(HCOO)_3$ (M = Fe, Ni and n = 0, 0.1) as absorber in PSCs. DFT calculations were utilized to used to examine the structural stability, band structure, and electronic contribution of the constituent elements, and the DD modeling was used to predict PSCs performance. The combination of DFT and DD model can incorporate defect formation (and hence degradation) and grain boundaries[40], and, therefore, can predict short and long-term performance degradation in PSCs. Overall, the integration of DFT with DD enables a multiscale simulation framework to captures both atomistic-level material properties and macroscopic device behavior, thereby enhancing the accuracy and predictive capability of perovskite solar cell simulations.

6.4 Machine learning for accelerating

Machine learning (ML) is emerging as a novel and powerful tool in material science thanks to its ability to (i) generate more expressive and lower dimensional representations of complex data and (ii) connect different classes of data in multimodality (e.g. text and images). Thus ML models can be used to connect very different data sets and to accelerate on the fly well-established numerical models. For example, ML techniques have achieved great success in Molecular Dynamics[165] to accelerate numerical simulations by generating force fields on the fly or making a smart sampling of the configurational space[166]. Similarly, in the last decade, new methods based on the synergy between numerical schemes, like Dynamical Mode Decomposition (DMD) or Koopman operators[167], have been refined and merged with data-driven methods to accelerate the simulation of partial and ordinary differential equations. All these methods are fundamentally aimed to simplify, reduce the dimensionality of the system or to accelerate current numerical simulations. Moreover, ML methods can be used to generate from simulation data surrogate models that can directly bypass the full simulation for input-output relations. An example of such a surrogate model is presented in[168], where a Gaussian model was used to generate a surrogate model for a kinetic Monte Carlo simulation of a supercapacitor. Overall, ML is emerging as a very powerful and versatile set of tools that can work in perfect synergy with current numerical models.

6.5 Interfacing experimental data

Machine Learning as a toolset has started to gain importance in the field of perovskite research and applications in analyzing and coupling experimental data. ML can be used for novel perovskite discovery, classification and characterization of samples, optimization of fabrication processes, and analysis of sample-related time series[169]. Li *et al.* have presented a method using Gaussian Processes to search for high-performing cubic perovskites[170]. Behara *et al.* published an ML-based classification approach for perovskite crystal structures[171]. Characterization of samples based on Machine Vision (MV), a subset of ML with images as the main focus, has also been demonstrated to investigate film homogeneity[172], grain characteristics[173] and some optoelectrical properties, such as bandgap and absorption behavior[174]. A promising workflow for the optimization of perovskite nanoplatelet syntheses using a mixture of ML models was reported by Lampe et al.[175]. Time series data methods were used by Kouroudis *et al.* to predict the long-term outdoor performance of perovskite solar cells[176]. While ML as a tool in perovskite material research is still relatively new, it has already demonstrated great promise due to its flexible use cases, relatively quick deployment, and fast and fairly accurate predictions. Additionally, new methods in the field

View Article Online
DOI: 10.1039/D5EL00040H

are still being developed, which may lead to the improvement of model performances in the future. The core problem hindering ML for experimental data is the lack of available and well-curated databases. Therefore, the amount of training data is limited and very small compared to more publicly known ML models, such as large language models or image generators. To address this core issue, the scientific community should discuss what data is relevant and how best to store it, for which the FAIR principle can serve as a guideline[177]. The use of automated experimentation setups may help with the rapid production of data and may also provide opportunities to couple ML models to the setup itself, either for on-the-fly characterization or optimization purposes.

Conclusions

Despite excellent power conversion efficiency of 27%, PSCs face persistent challenges including instability, current-voltage (J–V) hysteresis, and interfaces and grain boundary-induced performance degradation. Drift-diffusion (DD) modeling has proven to be a powerful tool for probing the complex charge transport, recombination mechanisms and ionic defect migration in PSCs, especially where experimental techniques fall short. However, conventional DD models often rely on oversimplified assumptions and lack the fidelity to capture dynamic phenomena such as role shape and size of grains, ionic-electronic interactions, and especially the degradation of PSCs. Simplified approximations can result in misinterpretation of the calculated data despite nicely fitting with J-V curves.

This review critically examines the evolution and limitations of DD modeling in PSCs, highlighting key areas where accuracy and predictive power can be improved. We explore strategies for incorporating sub-models for traps, recombination, grain boundaries, mobility, ionic-electronic interactions, photon recycling, and quantum effects, and emphasize the importance of integrating experimental to minimize approximations. The possibility to include degradation pathways and time/frequency domain analysis has been discussed to probe insight into instability. For the modeling parameters not directly accessible through experiments, the synergy between DD and Density Functional Theory (DFT) is discussed as a pathway to bridge atomistic and device-level simulations. Furthermore, the possibility to combine machine learning and interfacing experimental data has been presented to speed up the simulations and improve robustness and reliability. By mapping the evolution of DD modeling and identifying key areas for refinement, this work provides a foundation for future efforts to develop predictive, high-fidelity simulation tools for perovskite photovoltaics.

Author contributions

Both authors contributed to the conceptualization, literature review, manuscript writing, review and editing parts of the paper.

Conflicts of interest

There are no conflicts to declare.

Data availability

No primary research results, software, or code have been included and no new data were generated or analyzed as part of this review.

Acknowledgements

This work was financially supported by the Indian Institute of Technology Guwahati via grant no. SESESUGI-ITG01472AJSN001.

Notes and references

1 D. A. Egger, A. Bera, D. Cahen, G. Hodes, T. Kirchartz, L. Kronik, R. Lovrincic, A. M. Rappe, D. R. Reichman and O. Yaffe, *Adv. Mater.*, 2018, **30**, 1800691.
2 M. B. Johnston and L. M. Herz, *Acc. Chem. Res.*, 2016, **49**, 146–154.
3 J. S. Manser, J. A. Christians and P. V. Kamat, *Chem. Rev.*, 2016, **116**, 12956–13008.
4 NREL, *Solar Cell Efficiency Chart, Accessed on 08 July 2024*, 2024, `https://www.nrel.gov/pv/assets/pdfs/best-research-cell-efficiencies.pdf`.
5 Y. Zhou, L. M. Herz, A. K. Jen and M. Saliba, *Nature Energy*, 2022, **7**, 794–807.
6 T. S. Sherkar, C. Momblona, L. Gil-Escrig, H. J. Bolink and L. J. A. Koster, *Adv. Energy Mater.*, 2017, **7**, 1602432.
7 A. Sengupta, M. A. Afroz, B. Sharma, S. Choudhary, N. Pant, Y. Gulia, N. Pai, D. Angmo and S. Satapathi, *Sustainable Energy & Fuels*, 2025, **9**, 3999–4022.
8 M. I. H. Ansari, A. Qurashi and M. K. Nazeeruddin, *J. Photochem. Photobiol. C*, 2018, **35**, 1–24.
9 B. Conings, J. Drijkoningen, N. Gauquelin, A. Babayigit, J. D'Haen, L. D'Olieslaeger, A. Ethirajan, J. Verbeeck, J. Manca, E. Mosconi, F. De Angelis and H.-G. Boyen, *Adv. Energy Mater.*, 2015, **5**, 1500477.
10 E. H. Balaguera and J. Bisquert, *ACS Energy Letters*, 2024, **9**, 478–486.
11 S. Tammireddy, M. N. Lintangpradipto, O. Telschow, M. H. Futscher, B. Ehrler, O. M. Bakr, Y. Vaynzof and C. Deibel, *The Journal of Physical Chemistry Letters*, 2024, **15**, 1363–1372.
12 W. Peng, C. Aranda, O. M. Bakr, G. Garcia-Belmonte, J. Bisquert and A. Guerrero, *ACS Energy Lett.*, 2018, **3**, 1477–1481.
13 S. Reichert, Q. An, Y.-W. Woo, A. Walsh, Y. Vaynzof and C. Deibel, *Nature communications*, 2020, **11**, 6098.
14 C. Li, A. Guerrero, Y. Zhong, A. Gräser, C. A. M. Luna, J. Köhler, J. Bisquert, R. Hildner and S. Huettner, *Small*, 2017, **13**, 1701711.
15 G. De Moor, N. Charvin, C. Farha, T. Meyer, L. Perrin, E. Planes and L. Flandin, *Solar RRL*, 2024, **8**, 2300998.
16 A. Singh and A. Gagliardi, 2020 IEEE 20th International Conference on Nanotechnology (IEEE-NANO), 2020, pp. 227–232.
17 G. Richardson, S. E. O'Kane, R. G. Niemann, T. A. Peltola, J. M. Foster, P. J. Cameron and A. B. Walker, *Energy Environ.*

View Article Online
DOI: 10.1039/D5EL00040H

Sci., 2016, **9**, 1476–1485.

18 Z. S. Wang, Y. An, X. Ren, H. Zhang, Z. Huang, H.-L. Yip, Z. Huang and W. C. H. Choy, *Nature Communications*, 2024, **15**, 9647.

19 H. Baishya, R. D. Adhikari, M. J. Patel, D. Yadav, T. Sarmah, M. Alam, M. Kalita and P. K. Iyer, *Journal of Energy Chemistry*, 2024, **94**, 217–253.

20 Y. Cui, C. Chen, C. Li, L. Chen, S. S. Bista, X. Liu, Y. Li, R. A. Awni, Z. Song and Y. Yan, *ACS applied materials & interfaces*, 2020, **12**, 10588–10596.

21 W. Clarke, G. Richardson and P. Cameron, *Advanced Energy Materials*, 2024, 2400955.

22 L. Xu, R. Molaei Imenabadi, W. G. Vandenberghe and J. W. P. Hsu, *APL Mater.*, 2018, **6**, 036104.

23 P. Caprioglio, C. M. Wolff, O. J. Sandberg, A. Armin, B. Rech, S. Albrecht, D. Neher and M. Stolterfoht, *Adv. Energy Mater.*, 2020, **10**, 2000502.

24 A. Singh and A. Gagliardi, *EPJ Photovolt.*, 2021, **12**, 4.

25 K. T. Tanko, S. R. Raga, N. Vahedigharehchopogh, F. Baumann, M. Karimipour, R. A. Miranda-Gamboa and M. Lira-Cantú, *Solar RRL*, 2025, 202500162.

26 T. Y. Ahmed, D. A. Noori, K. K. Ahmed and S. B. Aziz, *Materials Science in Semiconductor Processing*, 2024, **178**, 108459.

27 B. Olyaeefar, S. Ahmadi-Kandjani and A. Asgari, *Sol. Energy Mater. Sol. Cells*, 2018, **180**, 76–82.

28 P. Saxena and N. E. Gorji, *IEEE J. Photovolt.*, 2019, **9**, 1693–1698.

29 A. Singh, F. Matteocci, H. Zhu, D. Rossi, S. Mejaouri, S. Cacovich, M. auf Der Maur, F. Sauvage, A. Gagliardi, M. Graetzel *et al.*, *Sol. RRL*, 2021, **5**, 2100277.

30 N. Rodkey, I. Gomar-Fernández, F. Ventosinos, C. Roldan-Carmona, L. J. A. Koster and H. J. Bolink, *ACS Energy Letters*, 2024, **9**, 927–933.

31 M. Singh, R. Kumar, V. Singh *et al.*, *Materials Research Express*, 2019, **6**, 115611.

32 T.-Y. Huang, C.-C. Li, Y.-H. Lai, X.-K. Gao, Y.-C. Huang, C.-C. Yang, T.-L. Wu and C.-S. Tan, *Solar RRL*, 2025, **9**, 2500181.

33 M. Kerara, A. Naas, A. Gueddim and O. Meglali, *Transactions on Electrical and Electronic Materials*, 2024, **25**, 665–673.

34 P. Calado, I. Gelmetti, B. Hilton, M. Azzouzi, J. Nelson and P. R. Barnes, *Journal of Computational Electronics*, 2022, **21**, 960–991.

35 N. E. Courtier, J. M. Cave, A. B. Walker, G. Richardson and J. M. Foster, *J. Comput. Electron.*, 2019, **18**, 1435–1449.

36 V. M. Le Corre, M. Stolterfoht, L. Perdigon Toro, M. Feuerstein, C. Wolff, L. Gil-Escrig, H. J. Bolink, D. Neher and L. J. A. Koster, *ACS Appl. Energy Mater.*, 2019, **2**, 6280–6287.

37 A. Singh, W. Kaiser and A. Gagliardi, *Sol. Energy Mater. Sol. Cells*, 2021, **221**, 110912.

38 R. Zhou, Y. Chen, L. Zhou, Y. Yao, Y. Liu, C. Wang, L. Niu and L. Chen, *Solar Energy Materials and Solar Cells*, 2024, **264**, 112616.

39 T. S. Sherkar, C. Momblona, L. Gil-Escrig, J. Ávila, M. Sessolo, H. J. Bolink and L. J. A. Koster, *ACS Energy Lett.*, 2017, **2**, 1214–1222.

40 W. Kaiser, K. Hussain, A. Singh, A. A. Alothman, D. Meggiolaro, A. Gagliardi, E. Mosconi and F. De Angelis, *J. Mater. Chem. A*, 2022, **10**, 24854–24865.

41 J. Zhang, S. Tang, M. Zhu, Z. Li, Z. Cheng, S. Xiang and Z. Zhang, *Energy & Environmental Materials*, 2024, e12696.

42 A.-F. Castro-Méndez, J. Hidalgo and J.-P. Correa-Baena, *Adv. Energy Mater.*, 2019, **9**, 1901489.

43 S. Jariwala, H. Sun, G. W. Adhyaksa, A. Lof, L. A. Muscarella, B. Ehrler, E. C. Garnett and D. S. Ginger, *Joule*, 2019, **3**, 3048–3060.

44 T. Zhang, H. Luo, M. Abdi-Jalebi, H. Chen and L. Zuo, *Information & Functional Materials*, 2024, **1**, 87–107.

45 A. Pecchia, D. Gentilini, D. Rossi, M. Auf der Maur and A. Di Carlo, *Nano letters*, 2016, **16**, 988–992.

46 D. Rossi, A. Pecchia, M. A. der Maur, T. Leonhard, H. Röhm, M. J. Hoffmann, A. Colsmann and A. D. Carlo, *Nano Energy*, 2018, **48**, 20–26.

47 D. Rossi, M. A. der Maur, A. Pecchia and A. Di Carlo, 2017 International Conference on Numerical Simulation of Optoelectronic Devices (NUSOD), 2017, pp. 21–22.

48 M. I. Hossain, A. M. Saleque, S. Ahmed, I. Saidjafarzoda, M. Shahiduzzaman, W. Qarony, D. Knipp, N. Biyikli and Y. H. Tsang, *Nano Energy*, 2021, **79**, 105400.

49 C. Gao, D. Du and W. Shen, *Carbon Neutrality*, 2022, **1**, 9.

50 K. Hussain and A. Gagliardi, *Sol. Energy*, 2022, **243**, 193–202.

51 M. T. Neukom, A. Schiller, S. Züfle, E. Knapp, J. Ávila, D. Pérez-del Rey, C. Dreessen, K. P. Zanoni, M. Sessolo, H. J. Bolink *et al.*, *ACS Appl. Mater. Interfaces*, 2019, **11**, 23320–23328.

52 P. Calado, A. M. Telford, D. Bryant, X. Li, J. Nelson, B. C. O'Regan and P. R. Barnes, *Nat. Commun.*, 2016, **7**, 13831.

53 W. Shockley and W. Read Jr, *Phys. Rev.*, 1952, **87**, 835.

54 R. Hall, *Phys. Rev.*, 1951, **83**, 228–228.

55 J. I. Pankove, *Optical processes in semiconductors*, Courier Corporation, 1975.

56 J. M. Ball, S. D. Stranks, M. T. Hörantner, S. Hüttner, W. Zhang, E. J. Crossland, I. Ramirez, M. Riede, M. B. Johnston, R. H. Friend and H. J. Snaith, *Energy Environ. Sci.*, 2015, **8**, 602–609.

57 N. Tessler and Y. Vaynzof, *ACS Energy Lett.*, 2020, **5**, 1260–1270.

58 L. Canil, T. Cramer, B. Fraboni, D. Ricciarelli, D. Meggiolaro *et al.*, *Energy Environ. Sci.*, 2021, **14**, 1429–1438.

59 P. Calado and P. R. Barnes, *Nat. Energy*, 2021, **6**, 589–591.

60 L. Lei, S. Zhang, S. Yang, X. Li, Y. Yu, Q. Wei, Z. Ni and M. Li, *Nanotechnology*, 2018, **29**, 255201.

61 R. Alkarsifi, J. Ackermann and O. Margeat, *J. Met., Mater. Miner.*, 2022, **32**, 1–22.

62 Q. An, F. Paulus, D. Becker-Koch, C. Cho, Q. Sun, A. Weu, S. Bitton, N. Tessler and Y. Vaynzof, *Matter*, 2021, **4**, 1683–1701.

63 J. Xing, Q. Wang, Q. Dong, Y. Yuan, Y. Fang and J. Huang,

View Article Online
DOI: 10.1039/D5EL00040H

Phys. Chem. Chem. Phys., 2016, **18**, 30484–30490.

64 Y. Shao, Y. Fang, T. Li, Q. Wang, Q. Dong, Y. Deng, Y. Yuan, H. Wei, M. Wang, A. Gruverman *et al.*, *Energy Environ. Sci.*, 2016, **9**, 1752–1759.

65 B. Roose, A. Ummadisingu, J.-P. Correa-Baena, M. Saliba, A. Hagfeldt, M. Graetzel, U. Steiner and A. Abate, *Nano Energy*, 2017, **39**, 24–29.

66 S. Iftiquar and J. Yi, *Mater. Sci. Semicond. Process.*, 2018, **79**, 46–52.

67 V. Nandal and P. R. Nair, *J. Appl. Phys.*, 2019, **125**, 173110.

68 W. Yao, S. Fang, Z. Hu, L. Huang, X. Liu, H. Zhang, J. Zhang and Y. Zhu, *Small*, 2022, **18**, 2105140.

69 P. Jia, L. Qin, D. Zhao, Y. Tang, B. Song, J. Guo, X. Li, L. Li, Q. Cui, Y. Hu *et al.*, *Adv. Funct. Mater.*, 2021, **31**, 2107125.

70 Z. Chu, M. Yang, P. Schulz, D. Wu, X. Ma, E. Seifert, L. Sun, X. Li, K. Zhu and K. Lai, *Nat. commun.*, 2017, **8**, 1–8.

71 P. You, G. Tang, J. Cao, D. Shen, T.-W. Ng, Z. Hawash, N. Wang, C.-K. Liu, W. Lu, Q. Tai *et al.*, *Light: Science & Applications*, 2021, **10**, 68.

72 A. Hajjiah, *Optical and Quantum Electronics*, 2025, **57**, 215.

73 M. Liu, M. Endo, A. Shimazaki, A. Wakamiya and Y. Tachibana, *ACS Appl. Energy Mater.*, 2018, **1**, 3722–3732.

74 D. Ramirez, K. Schutt, J. F. Montoya, S. Mesa, J. Lim, H. J. Snaith and F. Jaramillo, *J. Phys. Chem. C*, 2018, **122**, 21239–21247.

75 M. H. Mohammadi, M. Eskandari and D. Fathi, *Sci. Rep.*, 2023, **13**, 18584.

76 E. Ouabida, M. Kibbou, Z. Haman and A. Ainane, *Mater. Today Commun.*, 2023, **35**, 106354.

77 S. Haque, M. Alexandre, C. Baretzky, D. Rossi, F. De Rossi, A. T. Vicente, F. Brunetti, H. Águas, R. A. Ferreira, E. Fortunato *et al.*, *ACS Photonics*, 2022, **9**, 2408–2421.

78 F. Jahantigh and S. Bagher Ghorashi, *Nano*, 2019, **14**, 1950127.

79 X. Sun, R. Asadpour, W. Nie, A. D. Mohite and M. A. Alam, *IEEE J. Photovolt.*, 2015, **5**, 1389–1394.

80 P. K. Patel, *Sci. Rep.*, 2021, **11**, 3082.

81 A. Singh and A. Gagliardi, *Sol. Energy*, 2019, **187**, 39–46.

82 S. Gohri, J. Madan and R. Pandey, *J. Electron. Mater.*, 2024, 1–9.

83 A. Kumar, P. Sharma *et al.*, *Sol. Energy*, 2023, **259**, 63–71.

84 J. B. Patel, A. D. Wright, K. B. Lohmann, K. Peng, C. Q. Xia, J. M. Ball, N. K. Noel, T. W. Crothers, J. Wong-Leung, H. J. Snaith *et al.*, *Adv. Energy Mater.*, 2020, **10**, 1903653.

85 H. Bencherif and M. K. Hossain, *Sol. Energy*, 2022, **248**, 137–148.

86 V. Campanari, F. Martelli, A. Agresti, S. Pescetelli, N. Y. Nia, F. Di Giacomo, D. Catone, P. O'Keeffe, S. Turchini, B. Yang, J. Suo, A. Hagfeldt and A. Di Carlo, *Sol. RRL*, 2022, **6**, 2200049.

87 H. Phirke, S. Gharabeiki, A. Singh, A. Krishna, S. Siebentritt and A. Redinger, *APL Energy*, 2024, **2**, 016111.

88 R. García-Rodríguez, A. J. Riquelme, M. Cowley, K. Valadez-Villalobos, G. Oskam, L. J. Bennett, M. J. Wolf, L. Contreras-Bernal, P. J. Cameron, A. B. Walker *et al.*, *Energy Technol.*, 2022, **10**, 2200507.

89 C. M. Wolff, P. Caprioglio, M. Stolterfoht and D. Neher, *Adv. Mater.*, 2019, **31**, 1902762.

90 A. Krishna, V. Skorjanc, M. Dankl, J. Hieulle, H. Phirke, A. Singh, E. A. Alharbi, H. Zhang, F. Eickemeyer, S. M. Zakeeruddin *et al.*, *ACS Energy Lett.*, 2023, **8**, 3604–3613.

91 L. Wagner, P. Schygulla, J. P. Herterich, M. Elshamy, D. Bogachuk, S. Zouhair, S. Mastroianni, U. Würfel, Y. Liu, S. M. Zakeeruddin, M. Grätzel, A. Hinsch and S. W. Glunz, *Matter*, 2022, **5**, 2352–2364.

92 J. Xia, C. Liang, H. Gu, S. Mei, S. Li, N. Zhang, S. Chen, Y. Cai and G. Xing, *Energy Environ. Mater.*, 2023, **6**, e12296.

93 T. Yang, W. Zhao, X. Liu and S. Liu, *Adv. Energy Mater.*, 2023, **13**, 2204192.

94 S. Wang, H. Guo and Y. Wu, *Mater. Futures*, 2023, **2**, 012105.

95 C. Chen, S. Zhang, S. Wu, W. Zhang, H. Zhu, Z. Xiong, Y. Zhang and W. Chen, *RSC adv.*, 2017, **7**, 35819–35826.

96 N. Shibayama, H. Kanda, T. W. Kim, H. Segawa and S. Ito, *APL Mater.*, 2019, **7**, 031117.

97 S. Bitton and N. Tessler, *J. Mater. Chem. C*, 2021, **9**, 1888–1894.

98 L. Tian, W. E. Sha, H. Xie, D. Liu, T.-G. Sun, Y.-S. Xia and W. Chen, *J. Appl. Phys.*, 2024, **135**, 225703.

99 W. Zhu, S. Wang, X. Zhang, A. Wang, C. Wu and F. Hao, *Small*, 2022, **18**, 2105783.

100 G. Nagabhushana, R. Shivaramaiah and A. Navrotsky, *Proc. Natl. Acad. Sci.*, 2016, **113**, 7717–7721.

101 W.-J. Yin, T. Shi and Y. Yan, *Appl. Phys. Lett.*, 2014, **104**, 063903.

102 S. Srivastava, S. Ranjan, L. Yadav, T. Sharma, S. Choudhary, D. Agarwal, A. Singh, S. Satapathi, R. K. Gupta, A. Garg *et al.*, *Communications Materials*, 2023, **4**, 52.

103 D. Moia and J. Maier, *ACS Energy Lett.*, 2021, **6**, 1566–1576.

104 S. Reichert, J. Flemming, Q. An, Y. Vaynzof, J.-F. Pietschmann and C. Deibel, *Physical Review Applied*, 2020, **13**, 034018.

105 Q. Wali, M. Aamir, A. Ullah, F. J. Iftikhar, M. E. Khan, J. Akhtar and S. Yang, *Chem. Rec.*, 2022, **22**, e202100150.

106 P. Lopez-Varo, J. A. Jimenez-Tejada, M. Garcia-Rosell, J. A. Anta, S. Ravishankar, A. Bou and J. Bisquert, *ACS Energy Letters*, 2017, **2**, 1450–1453.

107 S. Bitton and N. Tessler, *Energy Environ. Sci.*, 2023, **16**, 2621–2628.

108 A. Schiller, S. Jenatsch, B. Blülle, M. A. Torre Cachafeiro, F. Ebadi, N. Kabir, M. Othman, C. M. Wolff, A. Hessler-Wyser, C. Ballif *et al.*, *The Journal of Physical Chemistry Letters*, 2024, **15**, 11252–11258.

109 M. Minbashi and E. Yazdani, *Scientific Reports*, 2022, **12**, 14916.

110 A. Gagliardi and A. Abate, *ACS Energy Lett.*, 2017, **3**, 163–169.

111 S. van Reenen, M. Kemerink and H. J. Snaith, *J. Phys. Chem. Lett.*, 2015, **6**, 3808–3814.

View Article Online
DOI: 10.1039/D5EL00040H

112 K. Domanski, B. Roose, T. Matsui, M. Saliba, S.-H. Turren-Cruz, J.-P. Correa-Baena, C. R. Carmona, G. Richardson, J. M. Foster, F. De Angelis, J. M. Ball, A. Petrozza, N. Mine, M. K. Nazeeruddin, W. Tress, M. Grätzel, U. Steiner, A. Hagfeldt and A. Abate, *Energy Environ. Sci.*, 2017, **10**, 604–613.

113 O. Almora, P. López-Varo, R. Escalante, J. Mohanraj, L. F. Marsal, S. Olthof and J. A. Anta, *Journal of Applied Physics*, 2024, **136**, 094502.

114 W. Zhang, V. M. Burlakov, D. J. Graham, T. Leijtens, A. Osherov, V. Bulović, H. J. Snaith, D. S. Ginger, S. D. Stranks *et al.*, *Nat. Commun.*, 2016, **7**, 11683.

115 T. Leijtens, S. D. Stranks, G. E. Eperon, R. Lindblad, E. M. Johansson, I. J. McPherson, H. Rensmo, J. M. Ball, M. M. Lee and H. J. Snaith, *ACS Nano*, 2014, **8**, 7147–7155.

116 S. Shao, M. Abdu-Aguye, T. S. Sherkar, H.-H. Fang, S. Adjokatse, G. t. Brink, B. J. Kooi, L. J. A. Koster and M. A. Loi, *Adv. Funct. Mater.*, 2016, **26**, 8094–8102.

117 J. Euvrard, Y. Yan and D. B. Mitzi, *Nature Reviews Materials*, 2021, **6**, 531–549.

118 L. M. Herz, *ACS Energy Lett.*, 2017, **2**, 1539–1548.

119 C. Motta, F. El-Mellouhi and S. Sanvito, *Sci. Rep.*, 2015, **5**, 12746.

120 O. G. Reid, M. Yang, N. Kopidakis, K. Zhu and G. Rumbles, *ACS Energy Lett.*, 2016, **1**, 561–565.

121 S.-J. Yoo and J.-J. Kim, *Macromol. Rapid Commun.*, 2015, **36**, 984–1000.

122 M. Cardona and Y. Y. Peter, *Fundamentals of semiconductors*, Springer, 3rd edn, 2007.

123 D. A. Neamen, *Semiconductor physics and devices*, McGraw-Hill, 2011.

124 A. Biewald, N. Giesbrecht, T. Bein, P. Docampo, A. Hartschuh and R. Ciesielski, *ACS Appl. Mater. Interfaces*, 2019, **11**, 20838–20844.

125 M. Z. Mayers, L. Z. Tan, D. A. Egger, A. M. Rappe and D. R. Reichman, *Nano Lett.*, 2018, **18**, 8041–8046.

126 T. J. Savenije, C. S. Ponseca Jr, L. Kunneman, M. Abdellah, K. Zheng, Y. Tian, Q. Zhu, S. E. Canton, I. G. Scheblykin, T. Pullerits *et al.*, *J. Phys. Chem. Lett.*, 2014, **5**, 2189–2194.

127 K. Anoop and T. Ahipa, *Solar Energy*, 2023, **263**, 111937.

128 A. Raj, M. Kumar and A. Anshul, *Materials Today Chemistry*, 2021, **22**, 100595.

129 G. Ren, W. Han, Y. Deng, W. Wu, Z. Li, J. Guo, H. Bao, C. Liu and W. Guo, *Journal of Materials Chemistry A*, 2021, **9**, 4589–4625.

130 Y. Xu, Y. Li, S. Li, F. Balestra, G. Ghibaudo, W. Li, Y.-F. Lin, H. Sun, J. Wan, X. Wang *et al.*, *Advanced Functional Materials*, 2020, **30**, 1904508.

131 Z. Bin, Z. Liu, Y. Qiu and L. Duan, *Advanced Optical Materials*, 2018, **6**, 1800536.

132 A. Mityashin, D. Cheyns, B. P. Rand and P. Heremans, *Applied Physics Letters*, 2012, **100**, 053305.

133 V. Arkhipov, E. Emelianova, P. Heremans and H. Bässler, *Phys. Rev. B*, 2005, **72**, 235202.

134 V. Arkhipov, P. Heremans, E. Emelianova and H. Baessler, *Phys. Rev. B*, 2005, **71**, 045214.

135 M. Koopmans, M. A. Leiviskä, J. Liu, J. Dong, L. Qiu, J. C. Hummelen, G. Portale, M. C. Heiber and L. J. A. Koster, *ACS Applied Materials & Interfaces*, 2020, **12**, 56222–56230.

136 G. Masetti, M. Severi and S. Solmi, *IEEE Trans. Electron Devices*, 1983, **30**, 764–769.

137 C. Lombardi, S. Manzini, A. Saporito and M. Vanzi, *IEEE Transactions on Computer-Aided Design of Integrated Circuits and Systems*, 1988, **7**, 1164–1171.

138 B. Maynard, Q. Long, E. A. Schiff, M. Yang, K. Zhu, R. Kottokkaran, H. Abbas and V. L. Dalal, *Appl. Phys. Lett.*, 2016, **108**, 173505.

139 N. K. Elangovan, R. Kannadasan, B. Beenarani, M. H. Alsharif, M.-K. Kim and Z. H. Inamul, *Energy Rep.*, 2024, **11**, 1171–1190.

140 N. Ahn and M. Choi, *Adv. Sci.*, 2024, **11**, 2306110.

141 S. Macpherson, T. A. Doherty, A. J. Winchester, S. Kosar, D. N. Johnstone, Y.-H. Chiang, K. Galkowski, M. Anaya, K. Frohna, A. N. Iqbal *et al.*, *Nature*, 2022, **607**, 294–300.

142 V. Nandal and P. R. Nair, *ACS nano*, 2017, **11**, 11505–11512.

143 J. A. McLeod and L. Liu, *J. Phys. Chem. Lett.*, 2018, **9**, 2411–2417.

144 L. Lanzetta, T. Webb, N. Zibouche, X. Liang, D. Ding, G. Min, R. J. Westbrook, B. Gaggio, T. J. Macdonald, M. S. Islam *et al.*, *Nat. commun.*, 2021, **12**, 1–11.

145 S. Kundu and T. L. Kelly, *EcoMat*, 2020, **2**, e12025.

146 F. Sacconi, M. A. der Maur, M. Povolotskyi, G. Romano, A. Pecchia, G. Penazzi, S. Bellocchio and A. Di Carlo, *TIBERCAD User Manual*, 2009.

147 Y. P. Varshni, *physica*, 1967, **34**, 149–154.

148 M. P. Lumb, M. A. Steiner, J. F. Geisz and R. J. Walters, *J. Appl. Phys.*, 2014, **116**, 194504.

149 U. Aeberhard, S. Zeder and B. Ruhstaller, *Sol. RRL*, 2024, **8**, 2400264.

150 S. Zeder, B. Ruhstaller and U. Aeberhard, *Physical Review Applied*, 2022, **17**, 014023.

151 C. Cho, Y.-W. Jang, S. Lee, Y. Vaynzof, M. Choi, J. H. Noh and K. Leo, *Science advances*, 2021, **7**, eabj1363.

152 A. Bou, H. Abolins, A. Ashoka, H. Cruanyes, A. Guerrero, F. Deschler and J. Bisquert, *ACS Energy Letters*, 2021, **6**, 2248–2255.

153 E. H. Balaguera and J. Bisquert, *Energy & Fuels*, 2025, **3**, 3638–3648.

154 A. Riquelme, L. J. Bennett, N. E. Courtier, M. J. Wolf, L. Contreras-Bernal, A. B. Walker, G. Richardson and J. A. Anta, *Nanoscale*, 2020, **12**, 17385–17398.

155 W. Clarke, P. Cameron and G. Richardson, *The Journal of Physical Chemistry Letters*, 2024, **15**, 11730–11736.

156 W. Koch and M. C. Holthausen, *A chemist's guide to density functional theory*, John Wiley & Sons, 2nd edn, 2015.

157 F. Giustino, *Materials modelling using density functional theory: properties and predictions*, Oxford University Press, 2014.

View Article Online
DOI: 10.1039/D5EL00040H

158 C.-J. Yu, *Journal of Physics: Energy*, 2019, **1**, 022001.
159 W.-J. Yin, T. Shi and Y. Yan, *Adv. mater. (Deerfield Beach, Fla.)*, 2014, **26**, 4653–4658.
160 X. Diao, Y. Diao, Y. Tang, G. Zhao, Q. Gu, Y. Xie, Y. Shi, P. Zhu and L. Zhang, *Sci. Rep.*, 2022, **12**, 12633.
161 R. K. Pingak, A. Harbi, M. Moutaabbid, A. Z. Johannes, N. U. J. Hauwali, M. Bukit, F. Nitti and M. Z. Ndii, *Mater. Res. Express*, 2023, **10**, 095507.
162 D. Meggiolaro and F. De Angelis, *ACS Energy Lett.*, 2018, **3**, 2206–2222.
163 K. D. Jayan and V. Sebastian, AIP Conf. Proc., 2019, p. 020036.
164 S. Marimuthu, S. Pandiaraj, M. Muthuramamoorthy, K. E. Alzahrani, A. N. Alodhayb, S. Pitchaimuthu and A. N. Grace, *Physical Chemistry Chemical Physics*, 2024, **26**, 4262–4277.
165 S. Batzner, A. Musaelian, L. Sun, M. Geiger, J. P. Mailoa, M. Kornbluth, N. Molinari, T. E. Smidt and B. Kozinsky, *Nat. commun.*, 2022, **13**, 2453.
166 G. A. Siddiqui, J. A. Stebani, D. Wragg, P.-S. Koutsourelakis, A. Casini and A. Gagliardi, *Chem. Eur. J.*, 2023, **29**, e202302375.
167 H. Arbabi and I. Mezic, *SIAM J. Appl. Dyn. Syst.*, 2017, **16**, 2096–2126.
168 I. Kouroudis, M. Gößwein and A. Gagliardi, *J. Phys. Chem. A*, 2023, **127**, 5967–5978.
169 F. Mayr, M. Harth, I. Kouroudis, M. Rinderle and A. Gagliardi, *J. Phys. Chem. Lett.*, 2022, **13**, 1940–1951.
170 Z. Li, L. E. Achenie and H. Xin, *ACS Catal.*, 2020, **10**, 4377–4384.
171 S. Behara, T. Poonawala and T. Thomas, *Comput. Mater. Sci.*, 2021, **188**, 110191.
172 N. Taherimakhsousi, B. P. MacLeod, F. G. Parlane, T. D. Morrissey, E. P. Booker, K. E. Dettelbach and C. P. Berlinguette, *npj Comput. Mater.*, 2020, **6**, 111.
173 Y. Zhang and Y. Zhou, *Acc. Mater. Res.*, 2023, **4**, 209–211.
174 Y. Liu, W. Yan, H. Zhu, Y. Tu, L. Guan and X. Tan, *Org. Electron.*, 2022, **101**, 106426.
175 C. Lampe, I. Kouroudis, M. Harth, S. Martin, A. Gagliardi and A. S. Urban, *Advanced Materials*, 2023, **35**, 2208772.
176 I. Kouroudis, K. T. Tanko, M. Karimipour, A. B. Ali, D. K. Kumar, V. Sudhakar, R. K. Gupta, I. Visoly-Fisher, M. Lira-Cantu and A. Gagliardi, *ACS Energy Lett.*, 2024, **9**, 1581–1586.
177 T. J. Jacobsson, A. Hultqvist, A. García-Fernández, A. Anand, A. Al-Ashouri, A. Hagfeldt, A. Crovetto, A. Abate, A. G. Ricciardulli, A. Vijayan *et al.*, *Nat. Energy*, 2022, **7**, 107–115.

No primary research results, software, or code have been included, and no new data were generated or analyzed as part of this review.

View Article Online
DOI: 10.1039/D5EL00040H

25-March-2025